



저작자표시-비영리-변경금지 2.0 대한민국

이용자는 아래의 조건을 따르는 경우에 한하여 자유롭게

- 이 저작물을 복제, 배포, 전송, 전시, 공연 및 방송할 수 있습니다.

다음과 같은 조건을 따라야 합니다:



저작자표시. 귀하는 원저작자를 표시하여야 합니다.



비영리. 귀하는 이 저작물을 영리 목적으로 이용할 수 없습니다.



변경금지. 귀하는 이 저작물을 개작, 변형 또는 가공할 수 없습니다.

- 귀하는, 이 저작물의 재이용이나 배포의 경우, 이 저작물에 적용된 이용허락조건을 명확하게 나타내어야 합니다.
- 저작권자로부터 별도의 허가를 받으면 이러한 조건들은 적용되지 않습니다.

저작권법에 따른 이용자의 권리는 위의 내용에 의하여 영향을 받지 않습니다.

이것은 [이용허락규약\(Legal Code\)](#)을 이해하기 쉽게 요약한 것입니다.

[Disclaimer](#)

Master's Thesis

**Uric acid sensing based on sandwich carbon
electrode sets decorated with gold nanoparticles**

Sanghee Jung

Department of Mechanical Engineering

Graduate School of UNIST

2020

**Uric acid sensing based on sandwich carbon
electrode sets decorated with gold
nanoparticles**

Sanghee Jung

Department of Mechanical Engineering

Graduate School of UNIST

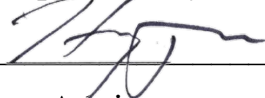
**Uric acid sensing based on sandwich carbon
electrode sets decorated with gold
nanoparticles**

A thesis submitted to the Graduate School of UNIST
in partial fulfillment of the
requirements for the degree of
Master of Science

Sanghee Jung

12/13/2019 of submission

Approved by



Advisor

Heungjoo Shin

Uric acid sensing based on sandwich carbon electrode sets decorated with gold nanoparticles

Sanghee Jung

This certifies that the thesis/dissertation of Sanghee Jung is approved.

12/13/2019

signature



Advisor: Heungjoo Shin

signature



Jaesung Jang

signature



Hoon Eui Jeong

Abstract

This study reports an enzymatic uric acid sensor with enhanced electrochemical sensing performance by electrodepositing gold nanoparticles on sandwich carbon electrodes. The improvement of sensor performance was based on the structural advantage of sandwich carbon electrode sets, consisting of suspended carbon mesh electrode (SME) and substrate bound interdigitated electrodes (IDE). The uricase enzyme was selectively immobilized to IDE and by-product generated from uricase-uric acid reaction was detected in SME to track the uric acid concentration. As the SME is completely covering the IDE, the by-product can be detected with SME before being diffused into the bulk solution.

The electrode structure was fabricated using simple and cost-effective technique known as carbon-microelectromechanical-systems (C-MEMS). The polymer structure was patterned using successive photolithography and converted into carbon electrode by vacuum pyrolysis. This unique technique enabled the wafer-level fabrication of two separate but adjacent electrodes; SME and IDE.

To enhance the surface reactivity and surface area of electrodes, gold nanoparticles were electrodeposited to the sandwich carbon electrodes. As the surface area of IDE is larger compared to the simple planar electrode, the electrodeposition of gold nanoparticles is improved on IDE.

The uricase enzyme was selectively immobilized to the IDE with selective electrochemical surface modification using aryl diazonium reduction. Uricase enzyme was selectively immobilized by bonding with diazonium deposited to IDE. The selective immobilization of enzyme allowed the maintenance of SME surface electroactivity.

Uric acid sensing performance was evaluated by conducting chronoamperometry test with the sensor structure for the uric acid concentration range of 0 to 1000 μM . From structural advantage of sandwich carbon electrodes and high electrochemical reactivity of gold nanoparticles, the developed uric acid sensor was capable of sensitive uric acid sensing with low lower limit of detection (LOD) of 6.25 μM . As uric acid concentration of healthy person's blood is ranged from 120 to 450 μM , the sensing range of this uric acid sensor is appropriate in detecting uric acid concentration in human blood. The sensitivity was calculated as change in current signal per uric acid concentration change divided with sensor operation area. The sandwich electrode structure showed high sensitivity with two linear ranges of uric acid concentration. The calculated sensitivity was 742.11 $\mu\text{A}\cdot\text{mM}^{-1}\cdot\text{cm}^{-2}$ for low concentration range (0 – 100 μM) and 553.26 $\mu\text{A}\cdot\text{mM}^{-1}\cdot\text{cm}^{-2}$ for high concentration range (100 – 1000 μM).

Contents

Abstract	5
Table of contents	6
List of figures	8
List of tables.....	12
I Introduction	
1.1 Importance of uric acid sensor	13
1.2 Conventional uric acid sensing methods.....	13
1.3 Different electrode structures used for electrochemical biosensing	20
1.4 Thesis outline.....	24
II Experimental Method & Materials	
2.1 Overall sandwich electrode uric acid sensor fabrication.....	25
2.2 Carbon-MEMS: Carbon sandwich electrode	26
2.3 Electrodeposition: Gold nanoparticles decorated carbon electrodes.....	27
2.4 Enzyme immobilization: Selective immobilization of Uricase enzyme	27
2.5 Experimental setup: Uric acid sensing.....	28
III Results & Discussion	
3.1 Characteristics of gold nanoparticle decorated sandwich carbon electrodes	
3.1.1 Pyrolyzed carbon sandwich electrodes	29
3.1.2 Gold nanoparticles decorated sandwich electrodes	31

3.1.3	Selectively immobilized enzyme.....	33
3.2	Structural benefit of sandwich electrodes compared to IDA	
3.2.1	COMSOL simulation result.....	35
3.2.2	Cyclic voltammetry experiment result.....	37
3.3	Gold nanoparticle electrodeposition optimization	
3.3.1	Electrodeposition condition.....	40
3.3.2	IDE as bottom electrode compared to planar electrode	41
3.4	Uric acid sensing performance of this work.....	44
IV	Conclusion.....	47
	Reference.....	49
	Acknowledgement.....	54

List of Figures

- Figure 1.** Schematic of catalytic reaction by uricase enzyme in the presence of uric acid. The byproduct of the reaction, hydrogen peroxide (H_2O_2) is used in detection.
- Figure 2.** The reaction schematic of enzymatic fluorescence uric acid sensor including uricase/HRP enzyme based on H_2O_2 -sensitive QDs. As hydrogen peroxide cause quenching effect on the QDs, the uric acid concentration is measured by monitoring the change of the QDs fluorescence. [12]
- Figure 3.** Schematic of non-enzymatic fluorescence uric acid detection mechanism. The fluorescence emission is deterred in presence of uric acid as it causes quenching effect to CdTe Qds. [13]
- Figure 4.** Schematic diagram of enzymatic UV detection of uric acid using catalytic oxidation of TMB. The oxidation of TMB is induced in presence of hydrogen peroxide and MoS_2 nanoflakes and change the solution color from white to blue. [17]
- Figure 5.** Schematic diagram of non-enzymatic UV detection of uric acid. The TMB is oxidized to TMB_{OX} by hydrogen peroxide but in the presence of uric acid in the solution, catalytic reaction to reduce TMB_{OX} to TMB is occurred by CoP nanosheet grown on Ni foam (NF). [18]
- Figure 6.** Schematic of non-enzymatic electrochemical sensor that can measure ascorbic acid, dopamine, and uric acid simultaneously. From the Au@Pd-RGO nanocomposites, the oxidation peaks and peak currents are well separated for ascorbic acid, dopamine and uric acid that three substances can be detected simultaneously. [19]
- Figure 7.** The various method of functionalization is possible with carbon nanotubes. [35]
- Figure 8.** Schematic of enzymatic sensor that used single walled carbon nanotube (SWNT) to incubate enzyme on glassy carbon electrode. The enzyme was pre-incubated with enzyme solution before being deposited on the electrode. [27]
- Figure 9.** Fabrication step of enzymatic glucose sensor which utilized the tip of carbon nanotube for

covalent bonding with glucose oxidase enzyme. [37]

Figure 10. Image of polymer and pyrolyzed interdigitated array electrode (IDA) by scanning electron microscopy (SEM). The volume of photoresist is extremely reduced from pyrolysis process. [39]

Figure 11. Schematic diagram of fabricated gold nanoparticle decorated carbon interdigitated electrodes (AuNP/carbon IDEs) and the sensing mechanism. One comb was used to immobilize cholestenone enzyme and the other comb was used to detect the current signal generated by $[\text{Fe}(\text{CN})_6]^{4-}$ produced from enzymatic reaction. [33]

Figure 12. Schematic of fabrication steps of enzymatic uric acid sensor based on gold nanoparticles decorated sandwich electrodes which is evaluated in this work. Fabrication includes carbon-MEMS technique, gold electrodeposition, and selective immobilization of uricase enzyme.

Figure 13. Schematic of selective enzyme immobilization. The immobilization includes reduction of diazotated CMA, activation of carboxyl acid group with EDC/NHS and covalent bonding between amino group of uricase enzyme with the activated carboxyl acid group.

Figure 14. Image by scanning electron microscopy (SEM) of sandwich electrode structure before and after pyrolysis. (Above: sandwich structure by SU-8 photoresist before pyrolysis / Below: sandwich structure by glassy carbon after pyrolysis) The geometry of the structure is transformed due to volume reduction of polymer during the pyrolysis process.

Figure 15. Cyclic voltammetry (CV) graph of carbon sandwich electrode with 10 mM $[\text{Fe}(\text{CN})_6]^{4-}$ solution. The single mode CV was conducted simultaneously on carbon bottom IDE and suspended carbon mesh that was scan from 0 to 0.6 V vs Ag/AgCl. The dual mode CV was conducted by posing 0 to 0.6 V scan on IDE as generator electrode and -0.3 V on collector current at suspended mesh electrode.

Figure 16. Image by scanning electron microscopy (SEM) of gold electrodeposited interdigitated electrode (IDE) by varying the nucleation voltage in gold electrodeposition from -1.0 to -1.3 V vs Ag/AgCl. As nucleation voltage was increased from -1.0 to -1.3V vs Ag/AgCl, the gold

nanoparticle was more conformally grown and the size of each particles are reduced.

Figure 17. Dual mode cyclic voltammetry (CV) graph of gold electrodeposited IDA. The dual mode current increase as high nucleation voltage was given and more conformal deposition of gold nanoparticles was done. In case of -1.0 and -1.1V vs Ag/AgCl nucleation voltage, the IDA electrodes were shorted due to massively grown gold particles.

Figure 18. Image by scanning electron microscopy (SEM) of gold nanoparticle decorated sandwich electrode structure. The gold particles were conformally deposited on both suspended mesh electrode and interdigitated electrode.

Figure 19. Cyclic voltammetry (CV) graph of gold electrodeposited sandwich electrode with 10 mM $[\text{Fe}(\text{CN})_6]^{4-}$ solution. The single mode CV was conducted simultaneously on bottom IDE and suspended carbon mesh that was scan from 0 to 0.6 V vs Ag/AgCl. The dual mode CV was conducted by posing 0 to 0.6 V scan on IDE as generator electrode and -0.3 V on collector current at suspended mesh electrode.

Figure 20. 4-carboxymethylaniline (CMA) reduction graph during electrodeposition to carbon IDA. (voltage sweep range: +0.5V to -1.0V; scan rate: 0.05mV/sec).

Figure 21. Cyclic voltammetry (CV) graph of surface modified carbon IDA with 10 mM $[\text{Fe}(\text{CN})_6]^{3-}$. The graph show change in CV reaction after each modification steps for both modifying and unmodifying electrodes. From the difference between two graph, selective immobilization of uricase enzyme is proved. Also the extreme current drop in modifying electrode CV graph show that surface reactivity is severely harmed after enzyme immobilization.

Figure 22. Plot of ferrocyanide concentration distribution (color distribution) and relative flux velocity (gray arrows) around the electrode surface. The different color can be interpreted in to ferrocyanide concentration in mM through color legend. The ferrocyanide transporation is mainly occurred between the generator and collector electrodes.

Figure 23. The total flux magnitude collected in collector electrode in plotted in terms of generator

potential to compare the redox cycling efficiency of two electrode structures.

Figure 24. Scanning electron microscopy (SEM) image of interdigitated array electrode and sandwich electrodes which show the geometry of electrode structures used in the experiments.

Figure 25. Dual mode cyclic voltammetry (CV) graph of interdigitated array (IDA) electrode and sandwich electrode (SE) for both carbon and gold electrodeposited electrodes. SE showed superior current level in CV despite the fact that IDA have larger sensor operation area.

Figure 26. Scanning electron microscopy (SEM) image of gold nanoparticle deposition result on IDE and planar electrode. Both electrodes experienced 20 seconds of -1.3V vs Ag/AgCl as nucleation step and 40 seconds of -0.9V vs Ag/AgCl as particles growth step. Gold particles were more reliably deposited on IDE.

Figure 27. Plot of ferrocyanide concentration distribution (color distribution) and relative flux velocity (gray arrows) around the electrode surface. The different color can be interpreted in to ferrocyanide concentration in mM through color legend. The ferrocyanide transportation is mainly occurred between the generator and collector electrodes.

Figure 28. The total flux magnitude collected in collector electrode in plotted in terms of generator potential to compare the redox cycling efficiency of two electrode structures.

Figure 29. Schematic of three different types of uric acid sensor structures. Type A is interdigitated array (IDA) structure with one comb selectively immobilized with uricase enzyme. Type B is sandwich electrode (SE) with uricase enzyme selectively immobilized to suspended mesh electrode (SME). Type C is SE with uricase enzyme selectively immobilized to interdigitated bottom electrode (IDE).

Figure 30. Amperometric current responses from three independent uric acid sensor structures are plotted in terms of uric acid concentration. (Black circles: IDA structure, type A; blue circles: SE structure with current signal sensed with IDE, type B; red circles: SE structure with current signal sensed with SME, type C)

List of Tables

Table 1. Comparison in IDA and SE structure in terms of geometry and CV properties.

Table 2. Comparison in sensing performance between three types of uric acid sensing structures. The sensing performance was evaluated with low limit of detection and sensitivity in uric acid detection.

I Introduction

1.1 Importance of uric acid sensor

Uric acid (UA) is the final product of human purine metabolism, which occurs by nucleic acid release after cell death. Compared to other mammals that produce urea or allantoin as final product of purine breakdown, humans have relatively high level of uric acid (200 μ M – 400 μ M) in the serum. The decomposed UA is excreted from human body through urination. UA was once thought as metabolic waste from nucleosides but now its role as antioxidants to protect damaged cells and neuronal structures is being studied. [1,2] Through the balance of production and disposal of UA, the concentration of UA in blood is maintained in certain level and function as antioxidants.

However, when the balance is collapsed, abnormal level of UA blood concentration may cause certain conditions or even severe diseases. In case of hyperuricemia, the excessive UA level in serum, may cause kidney stone, fatty liver. [2] High level of UA cause stress to the kidney where metabolism is held and may lead to malfunction. [3] Certain disease as gout and kidney stones are triggered directly from excessive uric acid that is crystallized inside the body. In case of hypouricemia, low UA level in serum, may cause disorder such as Parkinson's disease by lack of antioxidants. [4]

Moreover, UA concentration is the biomarker of showing rate of cell death as most of the UA is caused from breakdown of nucleosides of dead cells. [2] Checking the cell death is crucial in treating cancer with chemotherapy as human body go through tumor lysis syndrome (TLS) caused by the sudden massive death of the tumor cells. [3] By TLS, body suffers metabolic abnormalities by extreme UA level which could damage kidney and increase the risk of gout. [3] To prevent the possible side effects from TLS, checking the UA level of cancer patient is critical.

Therefore, detecting UA is required for clinical diagnosis and treatment of the disease or to prevent the possible symptoms.

1.2 Conventional uric acid sensing methods

There have been many attempts in various measuring methods to measure uric acid concentration in human serum or urine. According to the presence of enzyme the sensing method of biosensors can be categorized into enzymatic sensing and non-enzymatic sensing.

In case of uric acid sensing, uricase enzyme, in other words, urate oxidase, is used as enzyme to selectively detect uric acid. Uricase exists in the body of animals that further degrade uric acid to urea or allantoin as final product of purine metabolism. [2] Uric acid is degraded in to allantoin in the presence of uricase enzyme. For enzymatic sensing, the uricase enzyme is included in the sensing mechanism to convert uric acid to allantoin and produce carbon dioxide (CO₂) and hydrogen peroxide (H₂O₂) as byproducts (Figure 1). As carbon dioxide can exist even without the uricase reaction, hydrogen peroxide is used as target for detecting the enzyme reaction. The methods in collecting signal from hydrogen peroxide varies such as fluorescence detection from activated fluorescence chemical, electrochemical detection by collecting electrical property change generated by hydrogen peroxide reaction, and more.

Enzymes used in biosensors are show high selectivity to their target molecule as the catalytic reaction due to substrate specificity. At the same time, enzyme is sensitive to the surrounding conditions including temperature, pH, inhibitors, denaturing and chelating agents. [5] From this characteristic of enzyme, the enzymatic biosensor requires sensitive storage and operation condition but show high selectivity and less interference issue. [5] For enzymatic uric acid sensors, uric acid can be selectively detected as uric acid exclusively reacts with uricase enzyme.

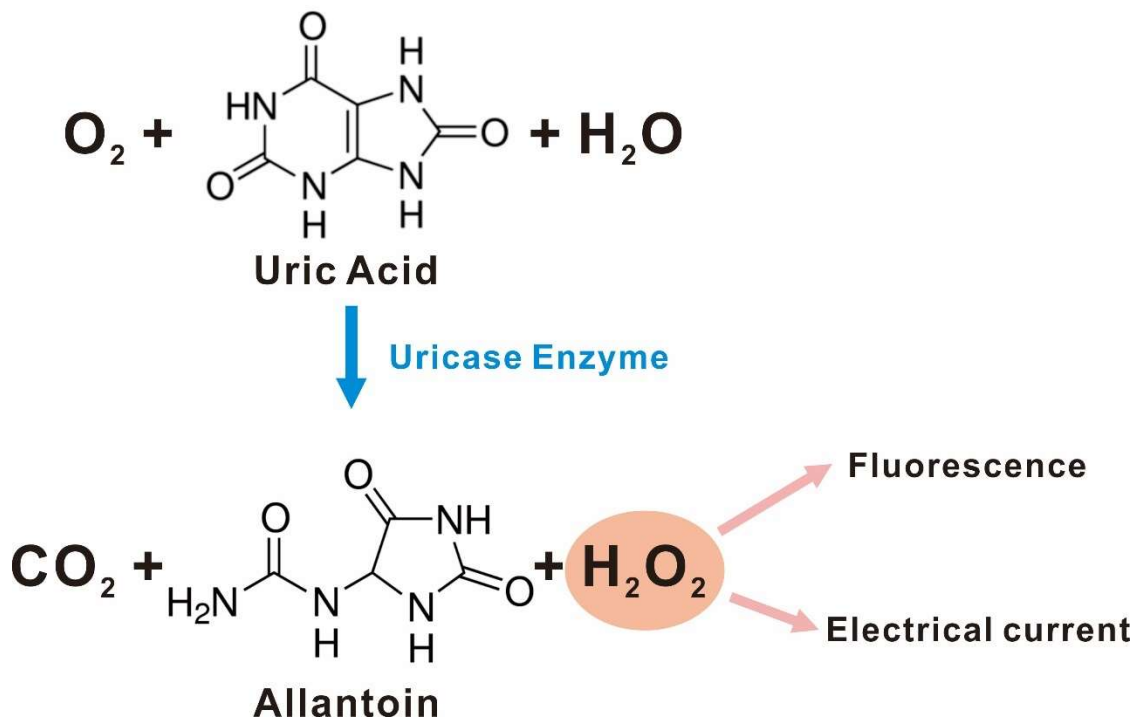


Figure 1. Schematic of catalytic reaction by uricase enzyme in the presence of uric acid. The byproduct of the reaction, hydrogen peroxide (H₂O₂) is used in detection.

- **Phosphotungstic detection**

The unique sensing method in uric acid sensor is to use phosphotungstic in uricase enzyme reaction. This method was first proposed in the mid-20th century which is counted as one of the early methods of uric acid detection. [6] A blue substance was observed from uric acid reaction under phosphotungstic acid and the phosphotungstic method in uric acid detection was proposed. [6] In phosphotungstic detection, phosphotungstic acid was oxidized in to tungsten blue, the blue substance observed, from uricase enzyme reaction instead of water molecule. [6-9] The amount of tungsten blue produced from enzyme reaction was quantified by spectrophotometry, to detect uric acid concentration.

There existed several problems with this phosphotungstic detection method. First, the cyanide solutions in phosphotungstic method were poisonous and relatively unstable. Also, the sensing method exhibited poor reproducibility and poor operability due to cloudy final reaction solution. [10] There was attempts to improve operability and stability of the phosphotungstic method by using single addition of phosphotungstic acid. [6] In this work, the color development was accelerated by heating at 100 °C for one minute.

- **Fluorescence detection**

Fluorescence detection method includes the reaction of fluorescence quenching, which refers to the decrease of fluorescence intensity induced from the presence of the target molecule, uric acid. The quenching could be cause by by-product of uricase enzyme reaction or uric acid itself depending on the substance used in the sensing mechanism. [11-14] The sensing mechanism of enzymatic uric acid sensor using fluorescence detection method is shown in Figure 2. The hydrogen peroxide, which is generated from enzymatic reaction by uric acid, cause another enzymatic reaction of HRP (Horseradish Peroxidase) and quench the fluorescence of carbon quantum dots. [12] Thus, fluorescence emission caused by quantum dot is reduced, allowing indirect detection of uric acid is possible through simple fluorescence detection. The sensing mechanism of non-enzymatic uric acid sensor which utilized direct quenching by uric acid was shown in Figure 3. [13] The hydrogen bond, formed between fluorescent group and uric acid lead to fluorescence quenching. [13, 15-16]

As the quenching can be interpreted as energy transfer of the molecule, it is very sensitive to pressure and temperature change. Therefore, to improve the accuracy of sensing result, ratio fluorescence method of using substance with multiple fluorescent emission peaks were tested.

[14] The co-doped NaYF₄ nanoparticles which have multiple emission peak were used as fluorescence emitting substance. Each emission peak was quenched independently that in presence of uric acid, fluorescence at 557 nm was quenched while the fluorescence at 705 nm remained identical. Therefore, in this work, the change in fluorescence ratio (I_{557}/I_{705}) showed uric acid concentration with less interference.

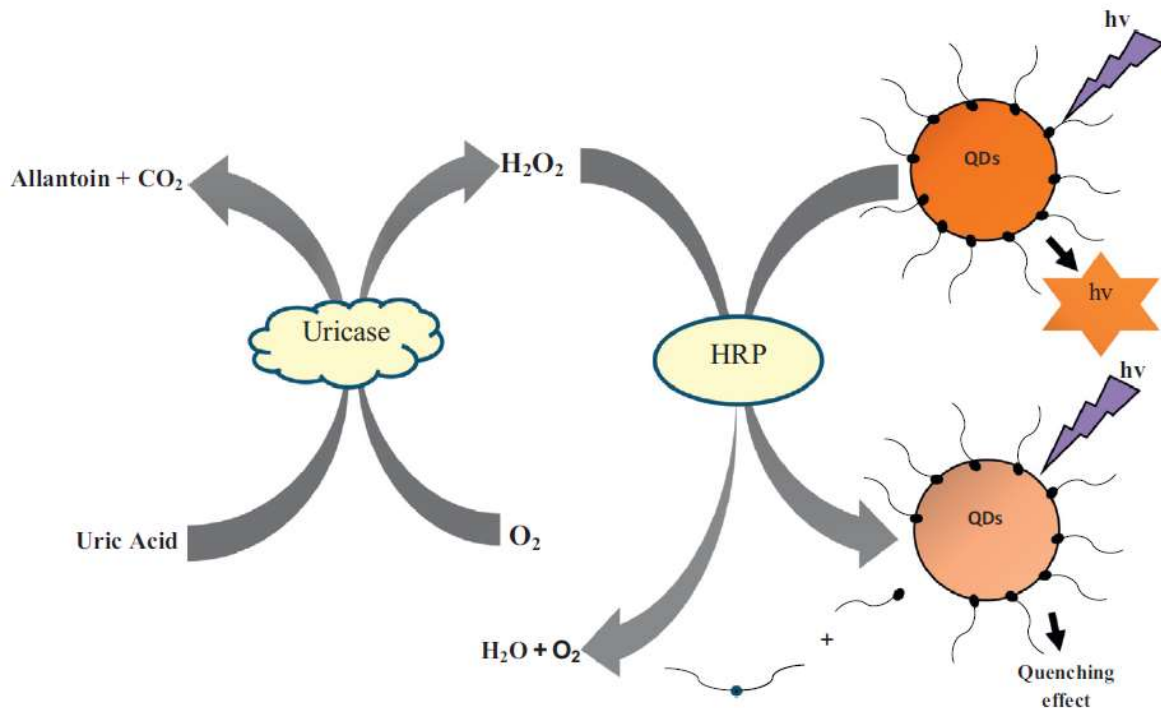


Figure 2. The reaction schematic of enzymatic fluorescence uric acid sensor including uricase/HRP enzyme based on H₂O₂-sensitive QDs. As hydrogen peroxide cause quenching effect on the QDs, the uric acid concentration is measured by monitoring the change of the QDs fluorescence. [12]

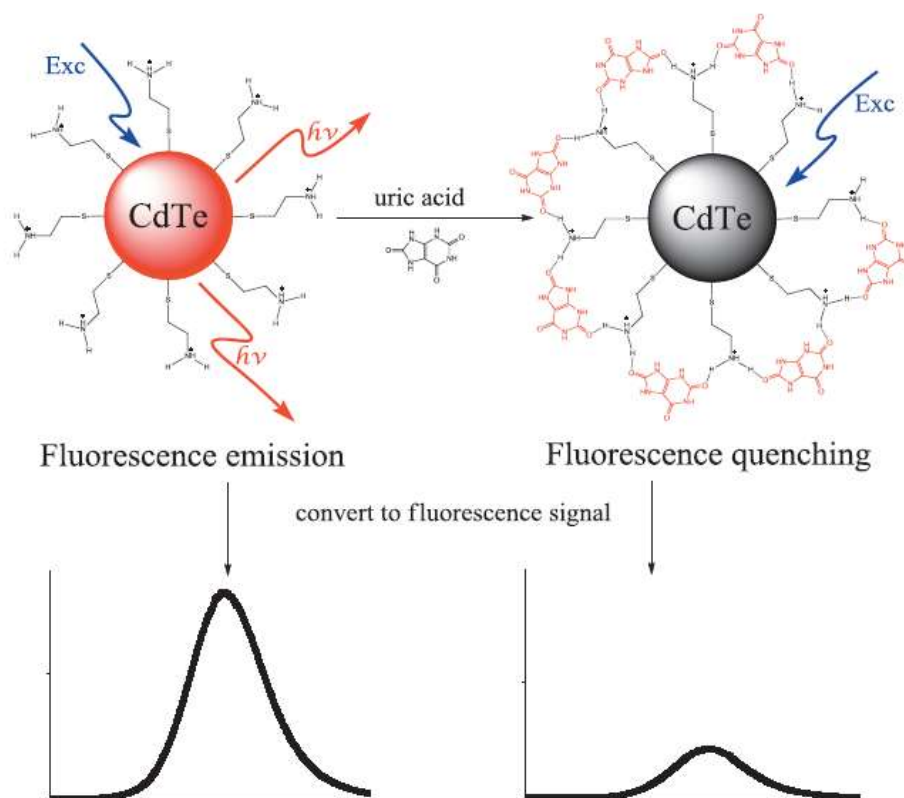


Figure 3. Schematic of non-enzymatic fluorescence uric acid detection mechanism. The fluorescence emission is deterred in presence of uric acid as it causes quenching effect to CdTe Qds. [13]

- UV detection

In UV detection in biosensing, TMB (3,3',5,5'-Tetramethylbenzidine) is commonly used as the H_2O_2 substrate to detect the presence of hydrogen peroxide. The oxidized TMB (TMB_{OX}) in the solution change the color of solution from white to blue, which can be measured with spectrophotometer for specific range of wavelength. The oxidation or reduction of TMB is used in uric acid detection to detect either hydrogen peroxide, which is produced by uricase reaction, that oxidizes TMB (Figure 4) or uric acid that reduces TMB_{OX} (Figure 5). [17, 18]

As shown in Figure 4, hydrogen peroxide is produced as a result of uric acid is oxidized by uricase enzyme. This specific team's work [17] is performed with the presence of MoS_2 nanoflakes which catalyze the TMB- H_2O_2 reaction, the hydrogen peroxide oxidizes the TMB and generate TMB_{OX} . This method measures the amount of hydrogen peroxide that is produced by the presence of uric acid. The uric acid is directly measured in Figure 5. [18] The existing hydrogen peroxide oxidizes TMB to TMB_{OX} with the catalytic help from CoP nanosheet arrays

grown on Ni foam (NF). The research team has found that uric acid reduces TMB_{OX} to TMB, deterring the color change by hydrogen peroxide. With this non-enzymatic sensing mechanism, measuring the suppressed color change shows the amount of uric acid in the solution.

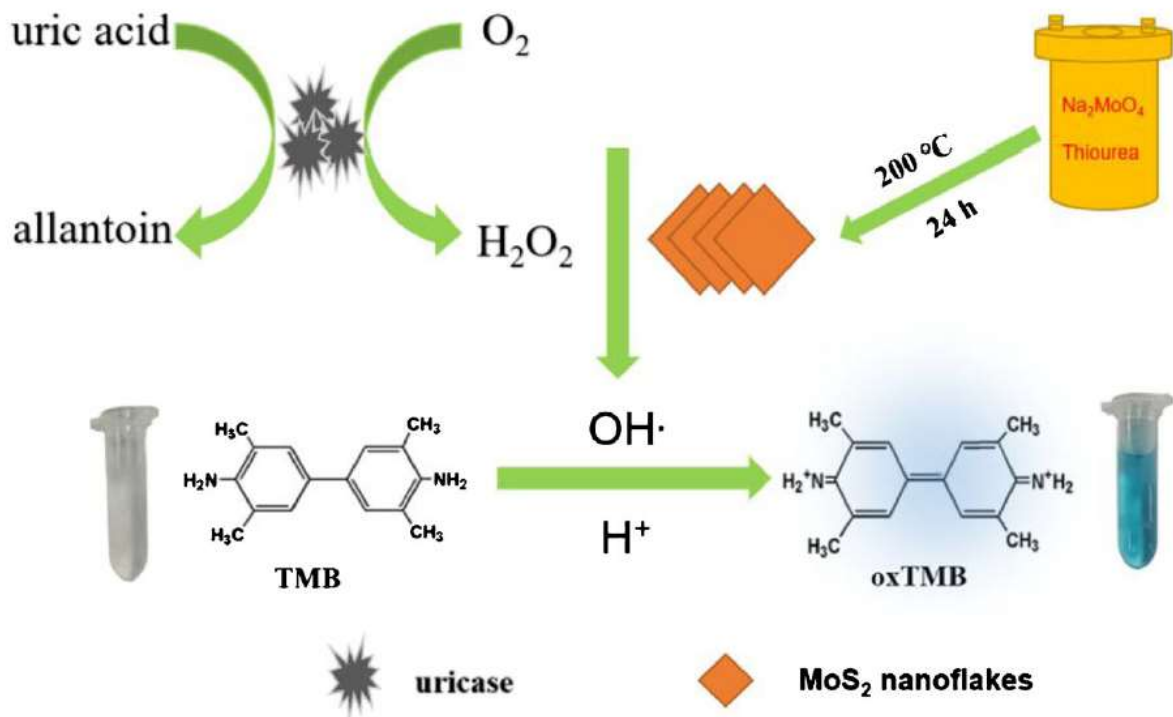


Figure 4. Schematic diagram of enzymatic UV detection of uric acid using catalytic oxidation of TMB. The oxidation of TMB is induced in presence of hydrogen peroxide and MoS_2 nanoflakes and change the solution color from white to blue. [17]

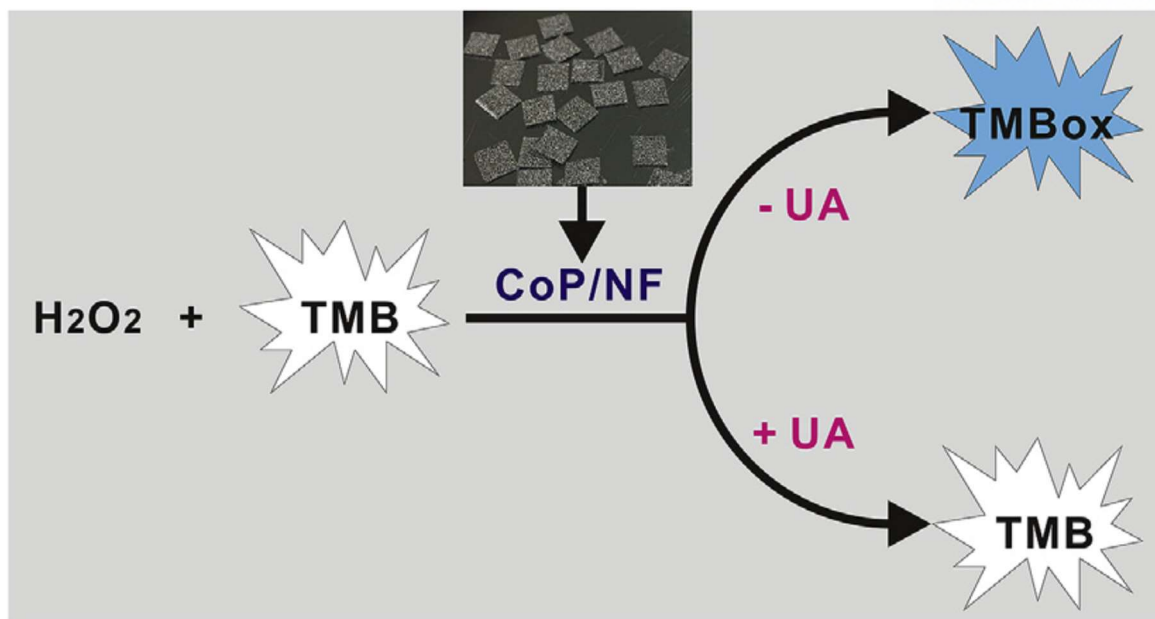


Figure 5. Schematic diagram of non-enzymatic UV detection of uric acid. The TMB is oxidized to TMB_{ox} by hydrogen peroxide but in the presence of uric acid in the solution, catalytic reaction to reduce TMB_{ox} to TMB is occurred by CoP nanosheet grown on Ni foam (NF). [18]

- Electrochemical detection

The electrochemical detection is one of the most common sensing methods chosen in biosensing due to its simplicity in operation method along with high signal response and short response time. Besides the presence of enzyme, the detection method may also vary by which electrical properties are being measured for the sensing mechanism. The measuring types include potentiometric sensor when potential difference is being recorded, amperometric sensor for collecting current signal, and impedance sensor when conductivity of the electrode is being measured.

For non-enzymatic electrochemical sensor, the target molecule, uric acid, is detected directly by the reaction on the electrode. Around 0.34V vs SCE, uric acid is oxidized directly on the electrode surface and current signal can be measured from the electron donated during the reaction. [19] The identification of uric acid concentration apart from other chemicals can be done as each molecule have their unique redox potential. To improve the performance of uric acid sensor, the electrode surface is modified with organic or inorganic materials that may even work as catalyst of uric acid oxidation.

The enzymatic electrochemical uric acid sensor includes uricase enzyme in their electrode. The sensor sensing mechanism is feasible with free enzyme in the solution but to improve the tolerance of uricase to surrounding conditions such as temperature and pH and the sensor performance in terms of sensitivity and selectivity, [20] most of the enzymatic electrochemical sensors have immobilized the enzyme to the surface of their sensor structure. The sensing mechanism of enzymatic uric acid sensor is to collect electron from hydrogen peroxide, which is generated from uric acid-uricase reaction. [21-23]

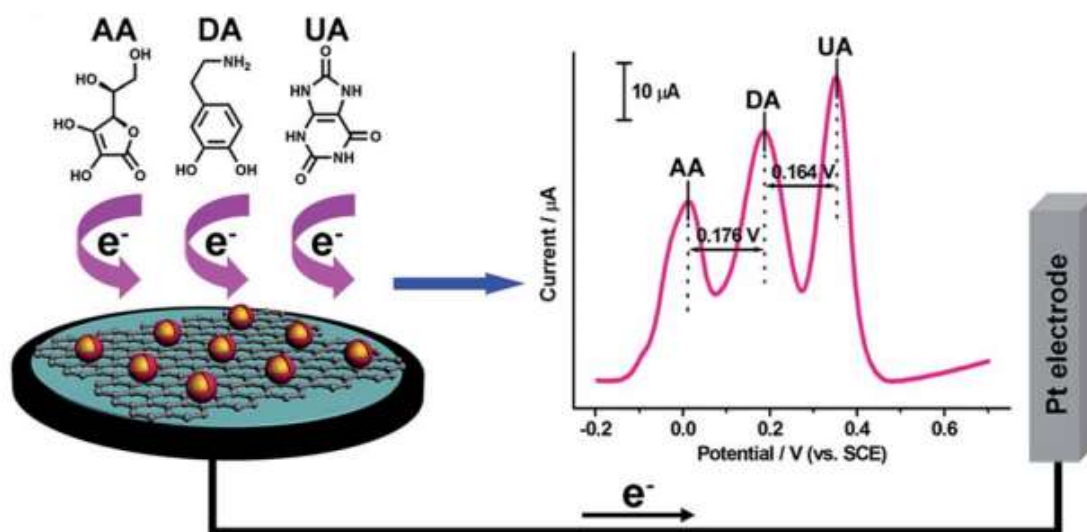


Figure 6 Schematic of non-enzymatic electrochemical sensor that can measure ascorbic acid, dopamine, and uric acid simultaneously. From the Au@Pd-RGO nanocomposites, the oxidation peaks and peak currents are well separated for ascorbic acid, dopamine and uric acid that three substances can be detected simultaneously. [19]

1.3 Different carbon structures used for electrochemical biosensing

The electrode structure in electrochemical biosensing differs depending on which sensing mechanism is being used for sensing target molecule. As carbon structure is likely to bond with organic substances by either direct or indirect covalent bonding, it is a good material to be used in biosensing where functionalization is necessary. There are various methods to utilize carbon structure in electrochemical biosensing including usage of micro carbon structure such as carbon nanotube and fullerene as the functionalized particle to be deposited

on electrode, [24-27, 29] usage of micro carbon structure as the linker to modify electrode surface, [28, 30-31] and fabricating the electrode in carbon. [32-34]

The micro carbon structures such as carbon nanotubes can be functionalized in various methods to match the needs. (Figure 7) For the biosensor, the substance that allows detection of target biomarker, such as enzyme, is bonded to the carbon structure. For fabricating enzymatic glucose sensor, single-walled carbon nanotube (SWNTs) was modified with glucose oxidase then cross-linking within a poly[(vinylpyridine)Os(bipyridyl)₂Cl^{2+/3+}] polymer film. [27] By depositing the functionalized SWNTs to the redox polymer films, the cyclic voltammetry current level was increased by 2 to 10 folds and glucose amperometric signal was three times amplified.

The micro carbon materials are also used as linker to bond proteins to the electrodes as the functional group can be activated with carbon materials. As shown in Figure 9, glucose oxidase was covalently immobilized to CNT nanoelectrode ensembles through carbodiimide reaction between their amine group of enzyme and carboxylic acid groups on the CNT tips. [37] The tip and side wall of CNT is well used as the linker to immobilize enzyme to the electrode. [35-37]

The carbon structure can be used as working electrode of biosensor. One of the conventional methods in fabricating carbon structure is using carbon-MEMS technique. [37] The carbon electrode structure is fabricated by pyrolyzing polymer structure which can be simply patterned with photolithography process. (Figure 10) The carbon-MEMS technique provides relatively simple but repeatable batch process. The carbon material produced by polymer pyrolysis is named glassy carbon and the material property varies by polymer property and pyrolysis condition. [38] The carbon interdigitated array electrode (carbon IDA) was fabricated by pyrolysis of SU-8 photoresist in Figure 11. [33] To enhance the surface reactivity, carbon surface was modified with gold nanoparticles and cholesterol oxidase was immobilized on the gold decorated carbon IDA.

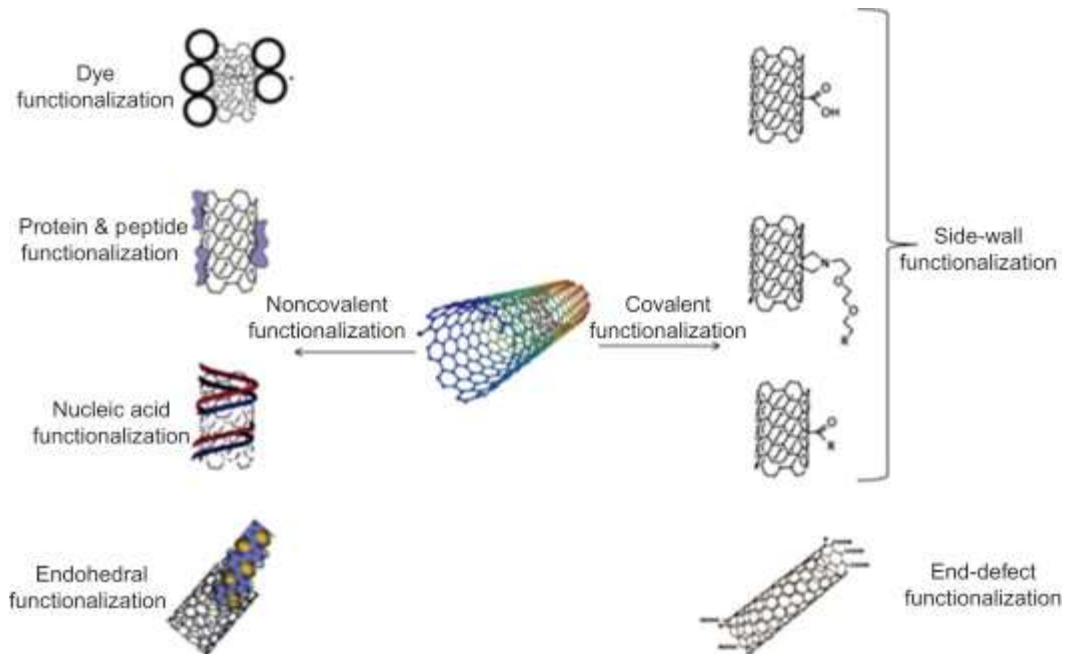


Figure 7. The various method of functionalization is possible with carbon nanotubes. [35]

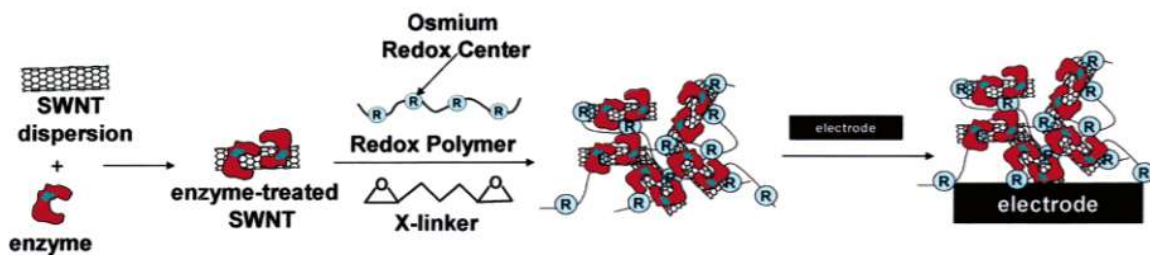


Figure 8. Schematic of enzymatic sensor that used single walled carbon nanotube (SWNT) to incubate enzyme on glassy carbon electrode. The enzyme was pre-incubated with enzyme solution before being deposited on the electrode. [27]

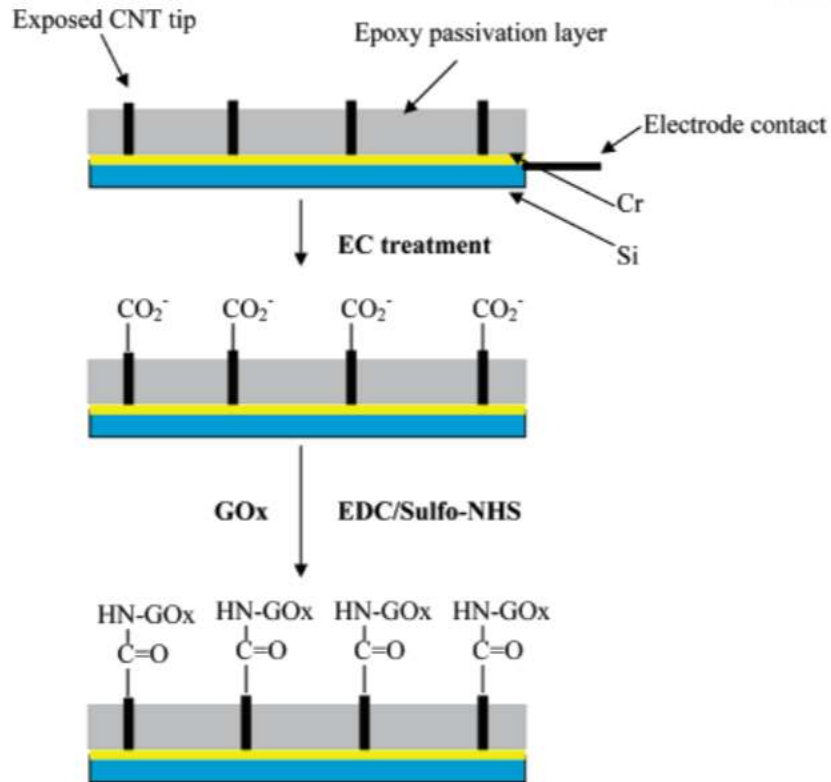


Figure 9. Fabrication step of enzymatic glucose sensor which utilized the tip of carbon nanotube for covalent bonding with glucose oxidase enzyme. [37]

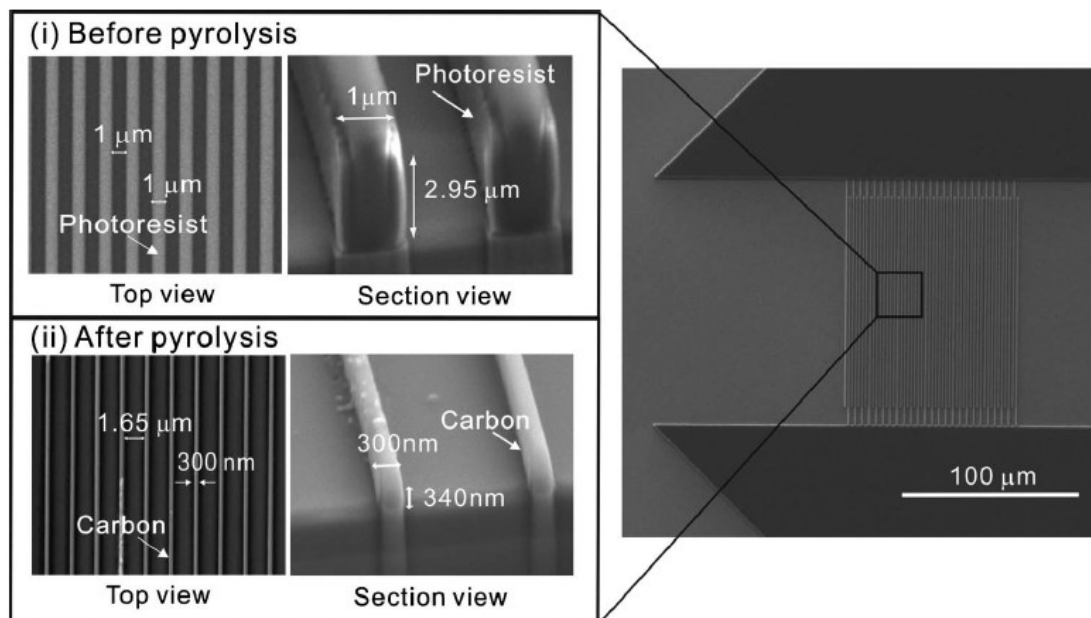


Figure 10. Image of polymer and pyrolyzed interdigitated array electrode (IDA) by scanning electron microscopy (SEM). The volume of photoresist is extremely reduced from pyrolysis process. [39]

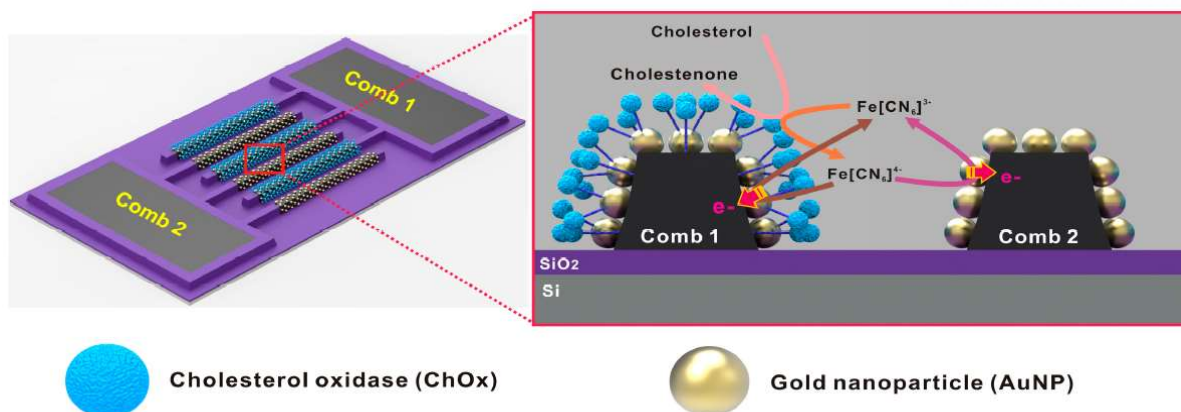


Figure 11. Schematic diagram of fabricated gold nanoparticle decorated carbon interdigitated electrodes (AuNP/carbon IDEs) and the sensing mechanism. One comb was used to immobilize cholesterol enzyme and the other comb was used to detect the current signal generated by $[\text{Fe}(\text{CN})_6]^{4-}$ produced from enzymatic reaction. [33]

1.4 Thesis outline

In this thesis, the details of uric acid sensor based on gold nanoparticles decorated sandwich electrodes is presented from fabrication to sensor evaluation. Sandwich structure consists of two independent electrodes; suspended mesh electrode and bottom electrode. The sandwich carbon electrodes structure was fabricated with batch process by using carbon-MEMS technique. Gold nanoparticles was electrodeposited over the carbon electrode to improve the surface reactivity of the electrode by increasing electrode surface area and improving the electroconductivity. Enzyme was selectively immobilized to bottom electrode to secure the reactivity of suspended mesh electrode where current signal from hydrogen peroxide will be collected.

The sensor structure was thoroughly evaluated by optimizing the details of the structure, such as bottom electrode type, and comparing the performance with interdigitated array electrode, which was previously treated in the lab. The final evaluation of the sensor was made with chronoamperometry detection result of uric acid concentration.

II Experimental Method & Materials

2.1 Overall sandwich electrode uric acid sensor fabrication

The fabrication of sandwich electrode uric acid sensor in this work can be defined in three steps. First, the carbon structure was fabricated with carbon-MEMS process, using UV photolithography and pyrolysis. Sandwich electrode structure was patterned with photolithography and turned into carbon electrode by pyrolysis process. To use the carbon electrode in electrochemical experiments, the SiO₂ insulation layer was patterned using PECVD and BOE etching. Second, to enhance the surface reactivity and surface area, gold nanoparticles were electrodeposited to the carbon electrode. Last, for uric acid sensing, uricase enzyme was selectively immobilized to gold nanoparticle decorated electrodes. The surface reactivity of sensing electrode was secured by selectively immobilizing the enzyme.

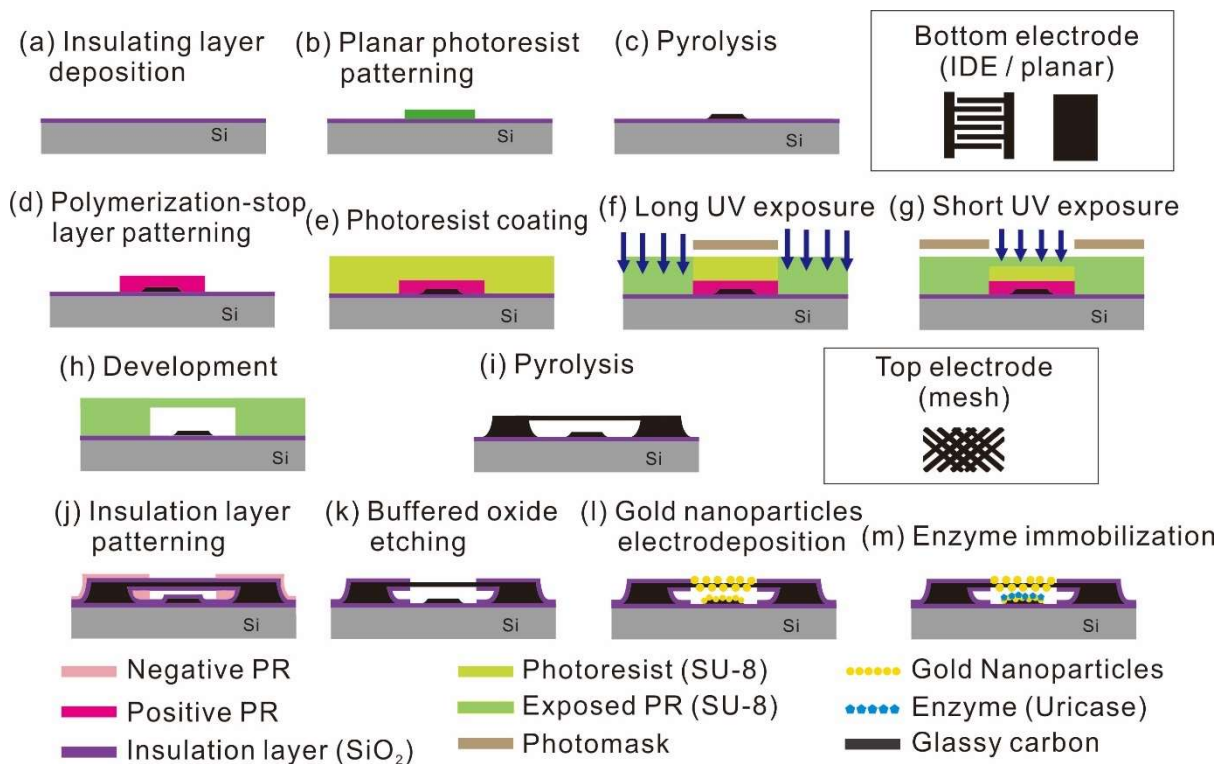


Figure 12. Schematic of fabrication steps of enzymatic uric acid sensor based on gold nanoparticles decorated sandwich electrodes which is evaluated in this work. Fabrication includes carbon-MEMS technique, gold electrodeposition, and selective immobilization of uricase enzyme.

2.2 Carbon-MEMS: Carbon sandwich electrode

The carbon sandwich electrodes were fabricated using Carbon MEMS, which is a technique to fabricate micro/nano scale patterned glassy carbon structure by pyrolyzing polymer structure of photoresist. Among different types of photoresists, SU8 photoresist was chosen to pattern polymer structure for its advantage in patterning high aspect ratio structure and sturdiness. The fabrication of carbon sandwich electrode structure is shown in step (a) to (k) of Figure 12.

To prevent the shortage of electrode structure through Si substrate of wafer, 1 μm -thick SiO_2 insulation layer was grown over the 6-inch Si wafer (p-type, boron doped, resistivity = 1-30 $\Omega\cdot\text{cm}$, thickness = 650-700 μm ; Silicon Technology Co., Ltd., Japan) through wet oxidation. On top of SiO_2 insulation layer, SU-8 negative photoresist (SU-8 2002, Microchem. Corp., USA) was successfully patterned to 2.5 μm -thick bottom IDE structure by UV photolithography. Then the polymer bottom IDE structure was pyrolyzed in vacuum rapid thermal annealing system (KVR-6000; Korea Vacuum Tech. Ltd., Daegu, Korea) up to 600°C to reduce the bottom IDE structure volume before patterning suspended mesh structure. A 6 μm -thick positive photoresist (DPR-i1549, Dongjin Semichem) was covered above pyrolyzed bottom IDE carbon structure as polymerization-stop layer to prevent suspended mesh structure being connected to bottom IDE structure. Then 17 μm -thick SU-8 negative photoresist (SU-8 2025, Microchem. Corp., USA) was spin-coated and patterned by two steps of UV exposure. First, high dose of UV-exposure of 220 mJ/cm^2 was given to pattern the post area of suspended mesh structure. Then, low dose of UV-exposure of 10 mJ/cm^2 was given to pattern the suspended mesh. After the careful post exposure bake and development of exposed SU-8 structure, 5 μm -thick suspended polymer mesh structure and 17 μm -thick posts structure was obtained. This polymer sandwich structures were pyrolyzed with vacuum furnace up to 920°C in 1°C/min temperature ramp rate. After pyrolysis, an oxygen plasma asher (PR Asher, KAMI, Germany) was used to remove the carbon residue on SiO_2 substrate. For the sandwich carbon electrodes to be used in electrochemical sensing, the 300nm SiO_2 insulation layer was deposition by PECVD (PEH-600, SORONA, Pyeongtaek, Korea) above carbon structures. The insulation open area was patterned with negative photoresist (NR5-8000, Futurrex Co., USA) and was opened by buffered oxide etching. After the buffered oxide etching, negative photoresist was removed with remover (RR41 remover, Futurrex Co., USA).

In characterizing the electrochemical reactivity of sandwich carbon electrode structure as a working electrode, cyclic voltammetry of 10mM $[\text{Fe}(\text{CN})_6]^{4-}$ (Potassium ferrocyanide; Sigma Aldrich Co., USA) was conducted in potentiostat (CHI1010, CH Instruments, Inc., USA) in potential range of 0 to 0.6 V vs Ag/AgCl at scan rate of 50mV/sec. For cyclic voltammetry, Ag/AgCl was used as reference electrode and platinum wire was used as counter electrode.

2.3 Electrodeposition: Gold nanoparticles decorated carbon electrodes

To enhance the surface reactivity and surface area, the gold nanoparticles were electrodeposited over the sandwich carbon electrodes using a potentiostat. 5mM gold solution was prepared as electrodeposition solution by diluting 16g/L Au thiosulfate-sulfite plating solution (TG Micro-500, T&I Chem Co. Ltd., Korea) in deionized (DI) water. The electrodeposition process was conducted in two steps; an initial step named nucleation step and following step named particles growth step. During nucleation step, high voltage was given to the glassy carbon electrodes to initiate the electrodeposition on carbon electrode. During particles growth step, relatively low voltage was given to the electrodes to grow the size of gold particles initiated during nucleation step. For this sandwich carbon electrodes, -1.3V vs. Ag/AgCl was given for 20 seconds as nucleation step and -0.9V vs. Ag/AgCl was given for 40 seconds as particles growth step.

2.4 Enzyme immobilization: Selective immobilization of Uricase enzyme

Selective immobilization was required in this work to secure the surface reactivity of sensing electrode. Selective immobilization of uricase enzyme to gold nanoparticles decorated carbon electrode was done in several steps as shown in Figure 13. [40, 41] First, for diazotation of 4-Aminophenylacetic acid (CMA, 98% purity; Sigma Aldrich Co., USA), CMA was mixed carefully with 15mM NaNO_2 and 15mM HCl in ice cold environment for 20 minutes which turned CMA to diazonium ion. The diazonium ion was electrodeposited on top of gold nanoparticles decorated carbon electrode. Electrodeposition was conducted by giving three cycles of cyclic voltammetry scan from 0.5 to -1.5V vs. Ag/AgCl in scan rate of 200mV/s with potentiostat. Then the electrode structure was rinsed with DI water and incubated in room temperature for 90 minutes in the presence of 0.1M N-(3-Dimethylaminopropyl)-N'-ethylcarbodiimide hydrochloride (EDC; Sigma Aldrich Co.,

USA) and 0.1M N-Hydroxysuccinimide (NHS, 98% purity; Sigma Aldrich Co., USA) solution. This step is to activate the carboxyl group of diazonium salt for final enzyme immobilization. After the incubation, the electrode structure was rinsed with DI water and incubated for 12 hours at 4°C under the presence of 4 mg/mL uricase enzyme (Uricase from *Candida sp.*; Sigma Aldrich Co., USA) solution in PBS (pH 7.5). The uricase enzyme is bound to EDC/NHS-activated electrodes, resulting in selective immobilization through following procedures.

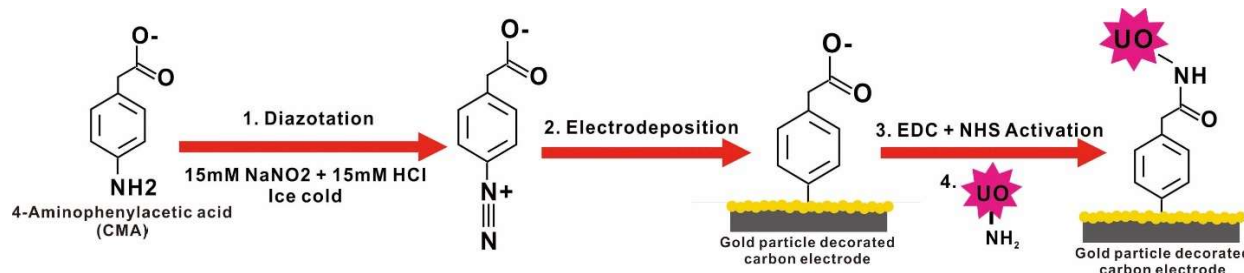


Figure 13. Schematic of selective enzyme immobilization. The immobilization includes reduction of diazotated CMA, activation of carboxyl acid group with EDC/NHS and covalent bonding between amino group of uricase enzyme with the activated carboxyl acid group.

2.5 Experimental setup: Uric acid sensing

To evaluate the property of uric acid sensor, uric acid concentration in PBS was measured according to concentration range from 0μM to 1000μM. 60mM uric acid stock solution was prepared by dissolving uric acid to 1M NaOH with enough sonication. The uric acid stock solution was diluted with PBS in preparing uric acid concentration solution without separate redox mediator. The uric acid sensing was conducted in chronoamperometric method of giving constant voltage of 0.6V vs Ag/AgCl to the sensing electrode for 100 seconds with potentiostat. The saturated current for each uric acid concentration experiment was recorded as the current signal for each uric acid concentration level. The sensing experiments were repeated 3 times.

III Results & Discussion

3.1 Characteristics of gold nanoparticle decorated sandwich carbon electrodes

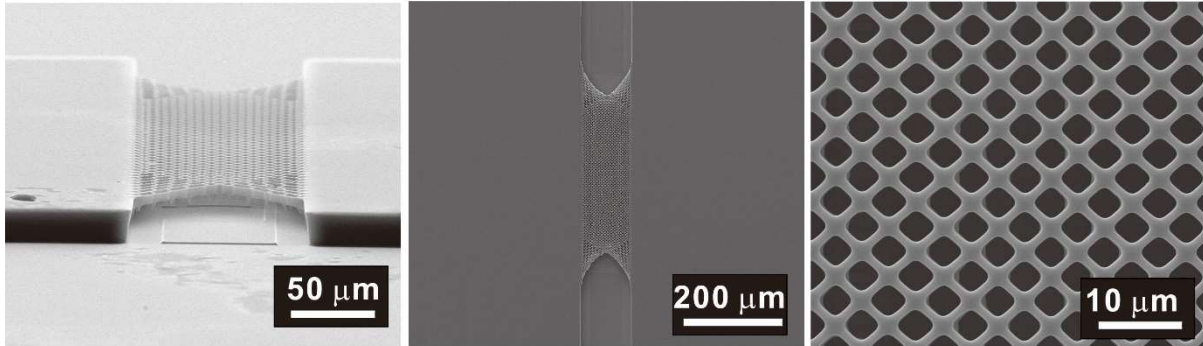
3.1.1 Pyrolyzed carbon sandwich electrodes

The photoresist patterned sandwich structure and pyrolyzed carbon sandwich electrodes are shown as scanning electron microscope (Quanta 200, FEI Company, USA) image in Figure 14. The height of bottom IDE structure is 2.5 μm before pyrolysis and turns to 500 nm after pyrolysis. The electrode gap between IDE is 1 μm for SU-8 structure but increase to 2 μm after pyrolysis. The height of the suspended mesh structure post is 17 μm and mesh thickness is 5 μm for SU-8 polymer structure but the overall volume of the structure shrinks after pyrolysis that height of the suspended mesh carbon electrode becomes 5 μm and carbon mesh thickness to 2 μm . As polymer post retrieve during pyrolysis, the width of suspended mesh increase from 100 μm to 130 μm . The electrode gap between suspended mesh carbon electrode and bottom IDE carbon electrode is 1.8 μm .

The sensor operation area, the electrode area which actually work for detecting uric acid concentration, is defined as the suspended mesh electrode area that overlap with bottom IDE. The width of sensing area is 70 μm and length of sensing area is 300 μm . Therefore, sensor operation area of the sandwich carbon electrodes is 21,000 μm^2 .

For electrochemical property, cyclic voltammetry (CV) of 10mM $[\text{Fe}(\text{CN})_6]^{4-}$ was conducted with Ag/AgCl reference electrode and platinum wire counter electrode using potentiostat. Two modes of cyclic voltammetry were done in this work; single mode and dual mode. The single mode CV is performed by giving two cycles of voltammetry scan from 0 to 0.6 V vs Ag/AgCl at scan rate of 50 mV/sec. The dual mode CV is performed by giving two cycles of voltammetry scan to generator electrode as in single mode CV and give constant voltage of -0.3V vs Ag/AgCl to collector electrode. This dual mode CV shows the redox cycling effectiveness of the electrode structure. The graph in Figure 15 shows CV graph of carbon sandwich electrode. The single mode CV of carbon bottom IDE showed current level of 0.191 μA and suspended carbon mesh showed current level of 0.852 μA at 0.6V vs Ag/AgCl. From dual mode CV with IDE as generator current, generator current showed current level of 5.068 μA and collector current at suspended mesh electrode showed current level of 4.975 μA at 0.6V vs Ag/AgCl.

Before pyrolysis



After pyrolysis

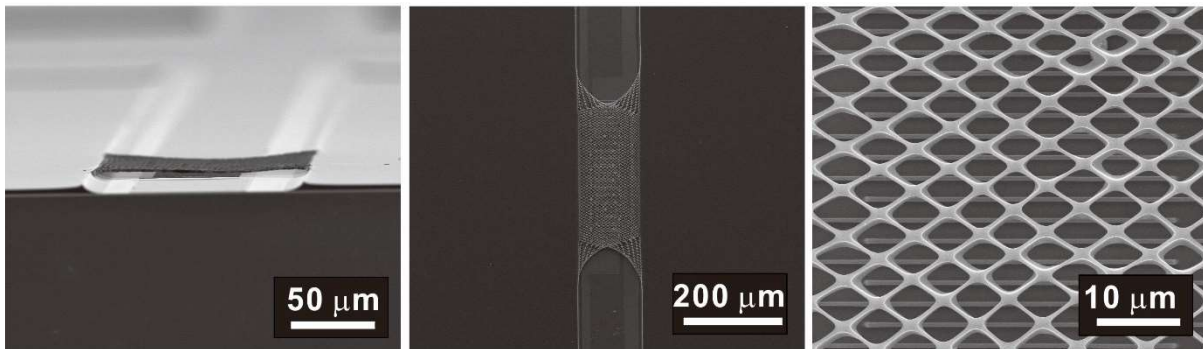


Figure 14. Image by scanning electron microscopy (SEM) of sandwich electrode structure before and after pyrolysis. (Above: sandwich structure by SU-8 photoresist before pyrolysis / Below: sandwich structure by glassy carbon after pyrolysis) The geometry of the structure is transformed due to volume reduction of polymer during the pyrolysis process.

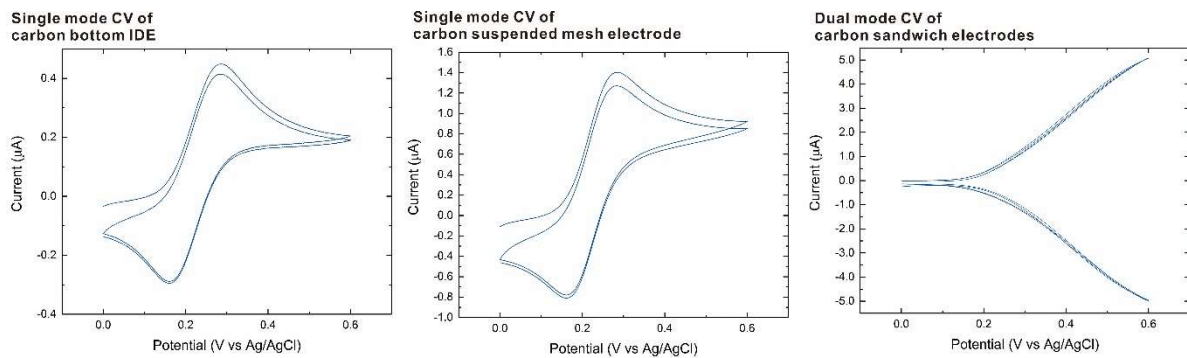


Figure 15. Cyclic voltammetry (CV) graph of carbon sandwich electrode with 10 mM $[\text{Fe}(\text{CN})_6]^{4-}$ solution. The single mode CV was conducted simultaneously on carbon bottom IDE and suspended carbon mesh that was scan from 0 to 0.6 V vs Ag/AgCl. The dual mode CV was conducted by posing 0 to 0.6 V scan on IDE as generator electrode and -0.3 V on collector current at suspended mesh electrode.

3.1.2 Gold nanoparticles decorated sandwich electrodes

The gold nanoparticles electrodeposition was done in two steps, nucleation and particle growth step. For better understanding of gold nanoparticles electrodeposition, the nucleation voltage amplitude was controlled and observed. This procedure was done in carbon interdigitated array (IDA) electrode which is also fabricated in Carbon MEMS technique. As nucleation voltage was increased from -1.0 to -1.3V vs Ag/AgCl, the gold nanoparticle was more conformally grown and the size of each particles are reduced (Figure 16). This result provides great explanation in the role of nucleation step. The role of nucleation step is to make seed layer of gold nanoparticles on carbon electrode with high potential. If the potential is not high enough, seed layer is not uniformly distributed across the carbon electrode, leading to limited number of gold particles deposition. Thus, during the particle growth step, the gold particle deposition is concentrated to those limited number of gold nanoparticle seed which cause massive growth to certain particles. However, if the nucleation potential is high enough, the gold nanoparticle seeds are conformally distributed and gold nanoparticles are uniformly enlarged. The electrochemical surface change due to gold nanoparticle deposition is shown in Figure 17. When nucleation potential was given as -1.0 and -1.1V vs Ag/AgCl, the IDA electrodes were shorted due to massively grown particles.

The carbon sandwich electrodes were decorated with gold nanoparticles by nucleation step of -1.3V vs Ag/AgCl for 20 seconds and particles growth step of -0.9V vs Ag/AgCl for 40 seconds. The gold nanoparticles, diameter of 200 – 300nm, are conformally deposited to both suspended mesh and bottom IDE.

The graph in Figure 19 shows CV graph of gold nanoparticles decorated sandwich electrode. The single mode CV of gold particle decorated IDE showed current level of 0.202 μA and gold particle decorated suspended mesh showed current level of 0.879 μA at 0.6V vs Ag/AgCl. From dual mode CV with IDE as generator current, generator current showed current level of 6.635 μA and collector current at suspended mesh electrode showed current level of 6.535 μA at 0.6V vs Ag/AgCl.

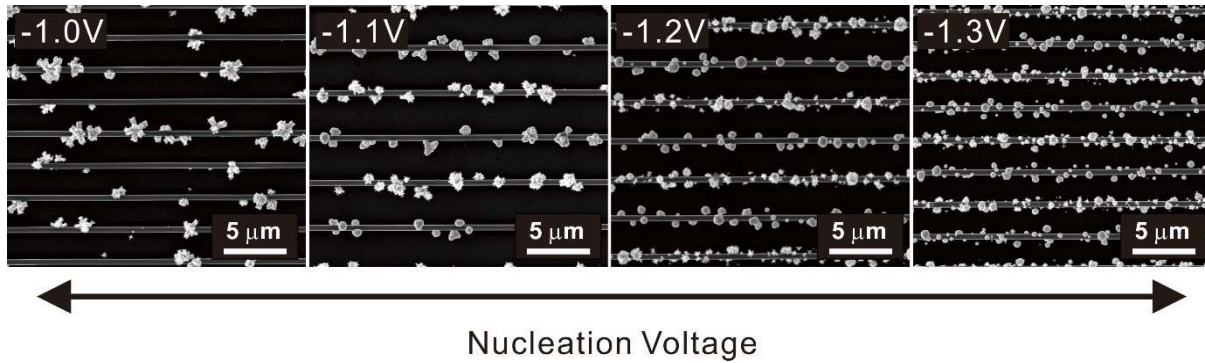


Figure 16. Image by scanning electron microscopy (SEM) of gold electrodeposited interdigitated electrode (IDE) by varying the nucleation voltage in gold electrodeposition from -1.0 to -1.3 V vs Ag/AgCl. As nucleation voltage was increased from -1.0 to -1.3V vs Ag/AgCl, the gold nanoparticle was more conformally grown and the size of each particles are reduced.

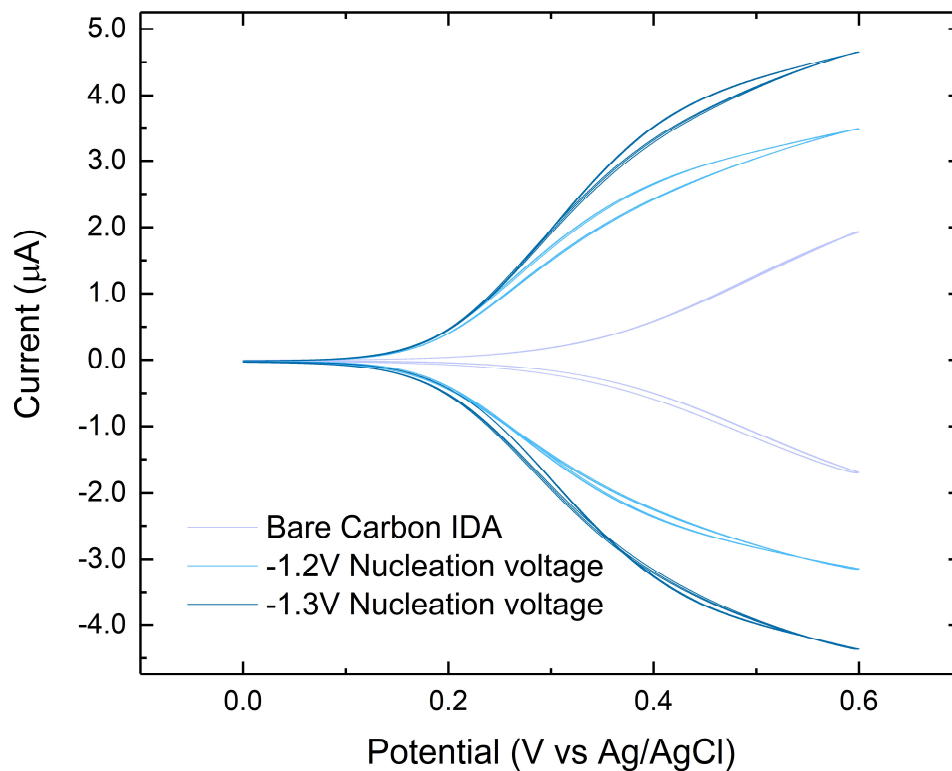


Figure 17. Dual mode cyclic voltammetry (CV) graph of gold electrodeposited IDA. The dual mode current increase as high nucleation voltage was given and more conformal deposition of gold nanoparticles was done. In case of -1.0 and -1.1V vs Ag/AgCl nucleation voltage, the IDA electrodes were shorted due to massively grown gold particles.

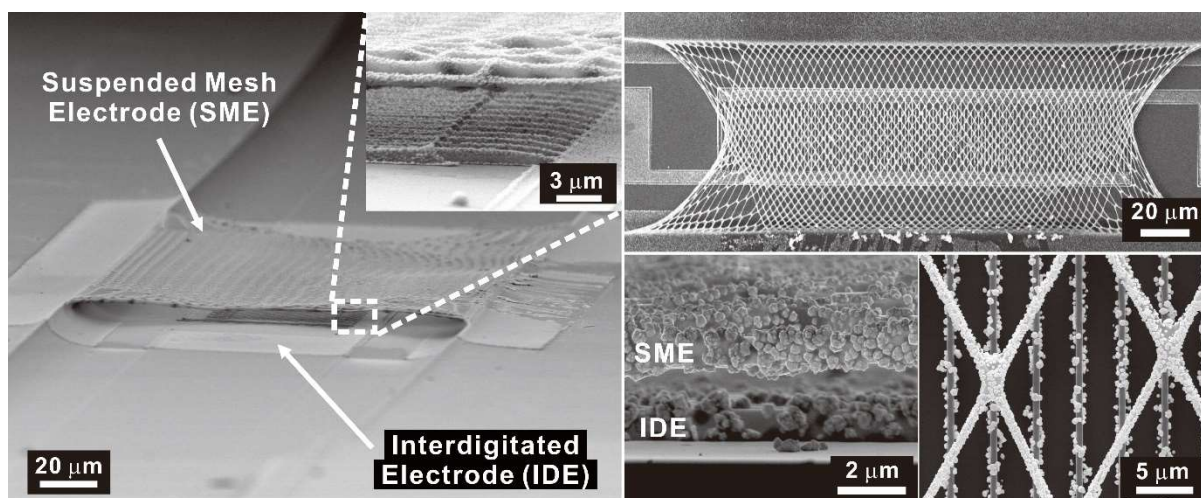


Figure 18. Image by scanning electron microscopy (SEM) of gold nanoparticle decorated sandwich electrode structure. The gold particles were conformally deposited on both suspended mesh electrode and interdigitated electrode.

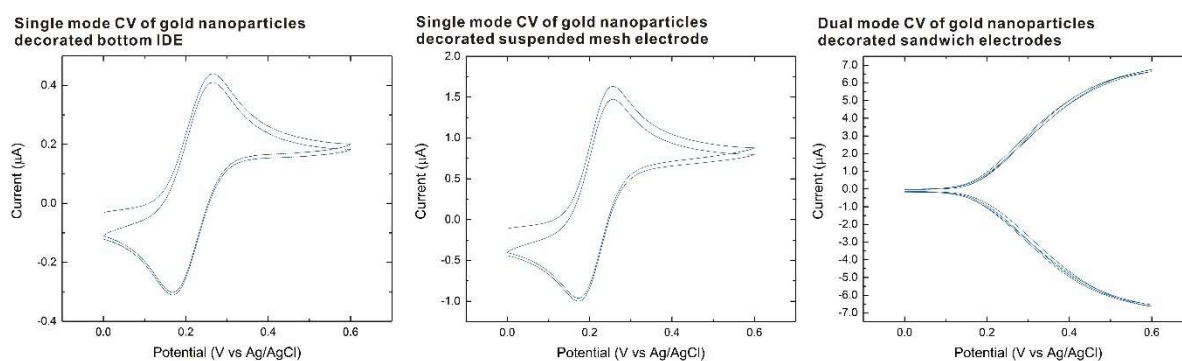


Figure 19 Cyclic voltammetry (CV) graph of gold electrodeposited sandwich electrode with 10 mM $[\text{Fe}(\text{CN})_6]^{4-}$ solution. The single mode CV was conducted simultaneously on bottom IDE and suspended carbon mesh that was scan from 0 to 0.6 V vs Ag/AgCl. The dual mode CV was conducted by posing 0 to 0.6 V scan on IDE as generator electrode and -0.3 V on collector current at suspended mesh electrode.

3.1.3 Selectively immobilized enzyme

The enzyme was selectively immobilized to either bottom IDE or suspended mesh electrode to maintain other electrodes as sensing electrode. This is possible as CMA can be selectively immobilized to certain electrode through electrodeposition. Figure 20 shows the reduction graph of CMA as three cycles of 0.5 to -1.0V vs Ag/AgCl

voltammetry scan was given the electrode. The difference between first cycle CV graph and second/third cycle CV graph shows that CMA reduction occurs during first voltammetry scan.

To see the surface reactivity change of the electrode surface, Figure 21 graph shows the 10mM $[\text{Fe}(\text{CN})_6]^{4-}$ CV graph of modifying and un-modifying electrode. As the progress of immobilization steps, the current level of the modifying electrode is significantly decreased but that of un-modifying electrode is barely decreased. This shows that electrode surface reactivity is significantly damaged by immobilizing the enzyme.

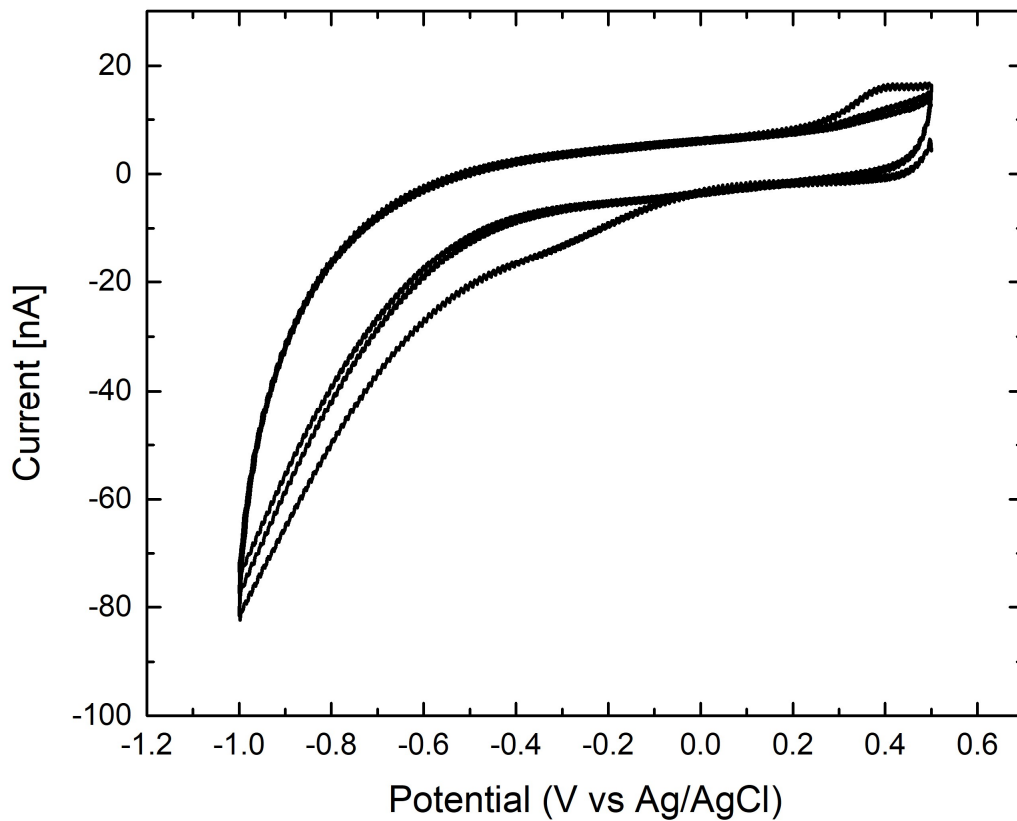


Figure 20. 4-carboxymethylaniline (CMA) reduction graph during electrodeposition to carbon IDA. (voltage sweep range: +0.5V to -1.0V; scan rate: 0.05mV/sec).

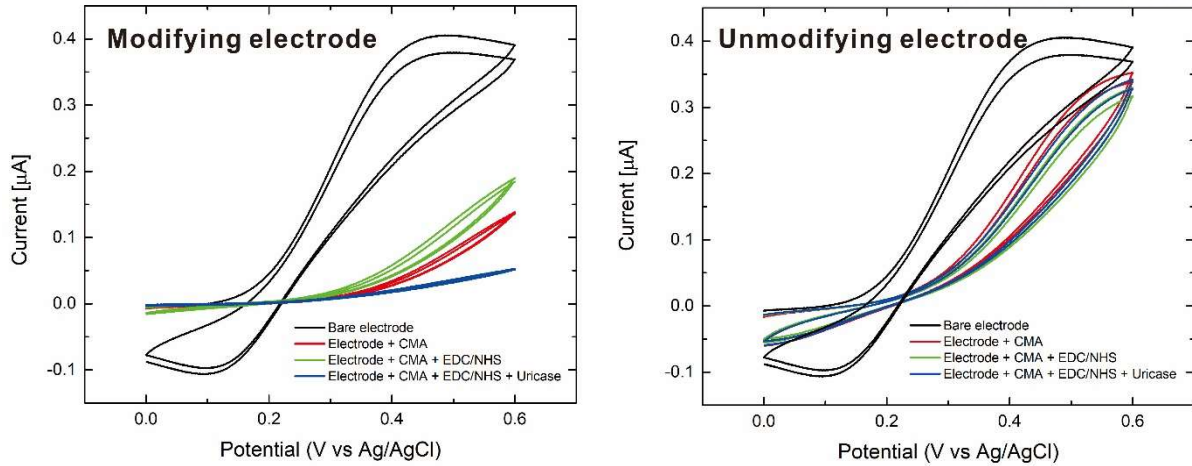


Figure 21. Cyclic voltammetry (CV) graph of surface modified carbon IDA with 10 mM $[\text{Fe}(\text{CN})_6]^{3-}$. The graph show change in CV reaction after each modification steps for both modifying and unmodifying electrodes. From the difference between two graph, selective immobilization of uricase enzyme is proved. Also the extreme current drop in modifying electrode CV graph show that surface reactivity is severely harmed after enzyme immobilization.

3.2 Structural benefit of sandwich electrodes compared to IDA

3.2.1 COMSOL simulation result

To compare structural benefit of sandwich electrode (SE) to interdigitated array (IDA), simulation was conducted using 2D flow simulation of COMSOL Multiphysics program. As the efficiency of electrode structures was meant to be compared in bulk solution, the simulation stage was set as large rectangle of width $10\mu\text{m}$ and height of $800\mu\text{m}$. At time $t = 0$, the bulk solution was filled with 10mM Ferrocyanide solution. The boundary condition of background top corner was set to show constant ferrocyanide concentration of 10mM. The surface of generator was calculated to remove ferrocyanide and replace it to ferricyanide according to ferrocyanide reaction speed, voltage applied to generator electrode and the adjacent ferrocyanide concentration to electrode surface. The surface of collector was calculated to remove ferricyanide and replace it to ferrocyanide according to ferricyanide reaction speed and the adjacent ferricyanide concentration to electrode surface. The mesh for simulation computation was formed in triangular shape (Element size = $0.001 - 3\mu\text{m}$, maximum element growth rate = 1.1, curvature factor = 0.2, resolution of narrow regions = 5). The simulation was conducted in time dependent computation in the range of 0 to 32

seconds which the time step of 0.1 seconds. The voltage scan was given to generator electrode from 0 to 0.8V with scan rate 0.05 V/s.

How the redox cycling between two electrodes are performed can be examined from ferrocyanide concentration distribution graph. As shown in Figure 22, ferrocyanide concentration, the redox cycling occurs in the area that is between generator and collector electrode. From IDA ferrocyanide concentration distribution graph, the redox cycling of IDA works in very limited area. In order to increase the redox cycling of IDA by increasing the electrode confronting area, the height of IDA electrode should be increased. However, to pattern IDA with small electrode gap without shortage if two combs, the height of the IDA is limited. For sandwich electrode, the redox cycling occurs all over the structure as generator and collector electrodes are facing each other for larger area, showing better redox cycling efficiency compared to IDA. The redox cycling efficiency was numerically measured by calculating total flux magnitude of collector electrode, which can be only resulted from redox cycling. As shown in Figure 23, the total flux magnitude of collector electrode is 14 nmol/(m·sec) for IDA and 19 nmol/(m·sec) for sandwich electrodes. This conclude that theoretically sandwich electrode shows better redox cycling efficiency than IDA.

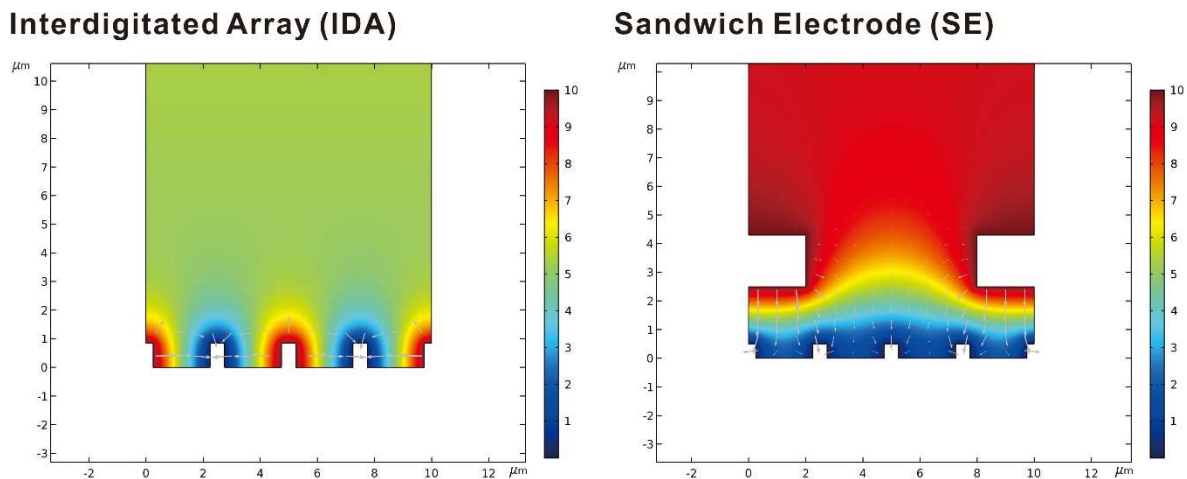
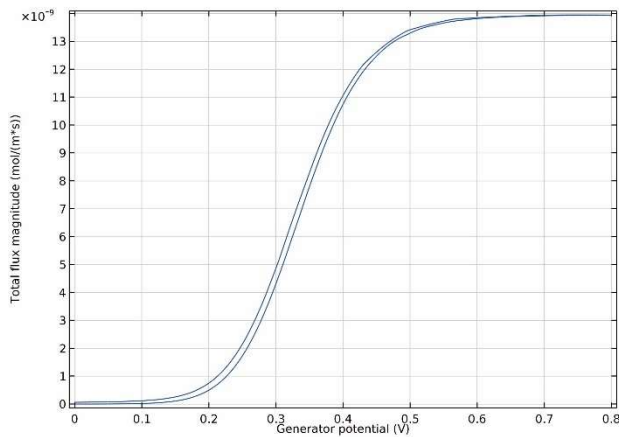


Figure 22. Plot of ferrocyanide concentration distribution (color distribution) and relative flux velocity (gray arrows) around the electrode surface. The different color can be interpreted in to ferrocyanide concentration in mM through color legend. The ferrocyanide transporation is mainly occurred between the generator and collector electrodes.

Interdigitated Array (IDA)



Sandwich Electrode (SE)

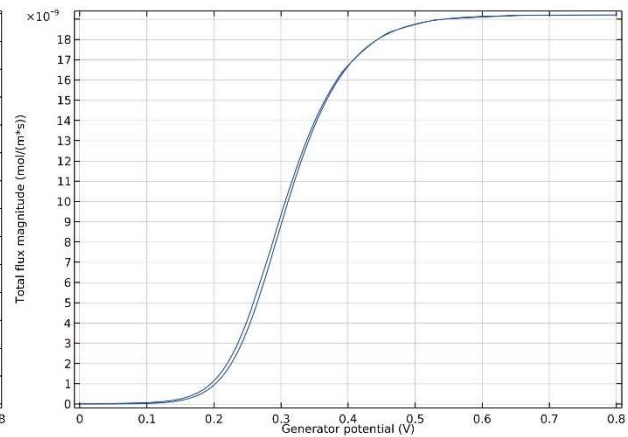


Figure 23. The total flux magnitude collected in collector electrode is plotted in terms of generator potential to compare the redox cycling efficiency of two electrode structures.

3.2.2 Experimental result

To confirm the structural superiority of sandwich electrodes (SE) compared to interdigitated array (IDA) electrodes, the actual geometry including sensing area and cyclic voltammetry test result of both electrode structures was compared. The IDA sensor structure, which was used in gold particle decorated IDA cholesterol sensor [33] was used to compare the property of gold particles decorated SE structure that was used in this work. The comparison is summarized in Table 1.

The material property of glassy carbon electrode was assumed to be similar as both structures are fabricated using carbon MEMS technique. The sensing area of IDA is calculated as $27,000 \mu\text{m}^2$ from insulation open area of IDA electrodes which is $90 \mu\text{m}$ -wide and $300 \mu\text{m}$ long. The sensing area of SE is calculated as $21,000 \mu\text{m}^2$ from the overlapping area of bottom IDE and suspended mesh which is $70 \mu\text{m}$ -wide and $300 \mu\text{m}$ -long. The electrode gap, which means the distance between generator electrode and collector electrode, is measured to be $2 \mu\text{m}$ in IDA carbon electrode and $1.8 \mu\text{m}$ in sandwich carbon electrode.

The redox cycling efficiency of electrode structure was compared with redox cycling current of collector electrode as it can be only resulted from redox cycling with generator electrode. The redox cycling current of collector current, shorten as redox cycling current, is 2.591 μA for carbon IDA structure and 5.065 μA for SE structure. Since the cyclic voltammetry current is proportional to electrode size, to surely compare the redox cycling efficiency, redox cycling current should be divided by sensor operation area. By calculating redox cycling efficiency, carbon SE structure (241.190 A/m^2) showed 2.51 times higher redox cycling efficiency compared to carbon IDA structure (95.963 A/m^2).

The redox cycling current increase when gold nanoparticles are deposited to electrodes. After gold nanoparticle deposition, redox cycling current increase by 79.6% for IDA structure (4.653 μA) and 31.0% for SE structure (6.635 μA). The redox cycling efficiency increment due to gold nanoparticle electrodeposition was greater on IDA. During pyrolysis, the distance between IDA combs increase as photoresist structure volume is reduced. Although the structure volume is reduced when turning in to carbon, there is very shallow layer of pyrolyzed carbon left as the trace of photoresist structure. This shallow carbon structure is barely used for bare carbon electrode structure due to high electrical resistance and can be ignored. However, high nucleation voltage allows gold nanoparticle to be electrodeposited on to this area and significantly reduce the electrode gap between two IDA combs. Therefore, structure efficiency enhancement by gold nanoparticle deposition is higher with IDA structure but the calculated redox cycling efficiency of gold nanoparticle decorated SE structure (315.952 A/m^2) showed 1.833 times higher rate compared to that of carbon IDA structure (172.333 A/m^2).

Interdigitated Array (IDA) Sandwich Electrode (SE)

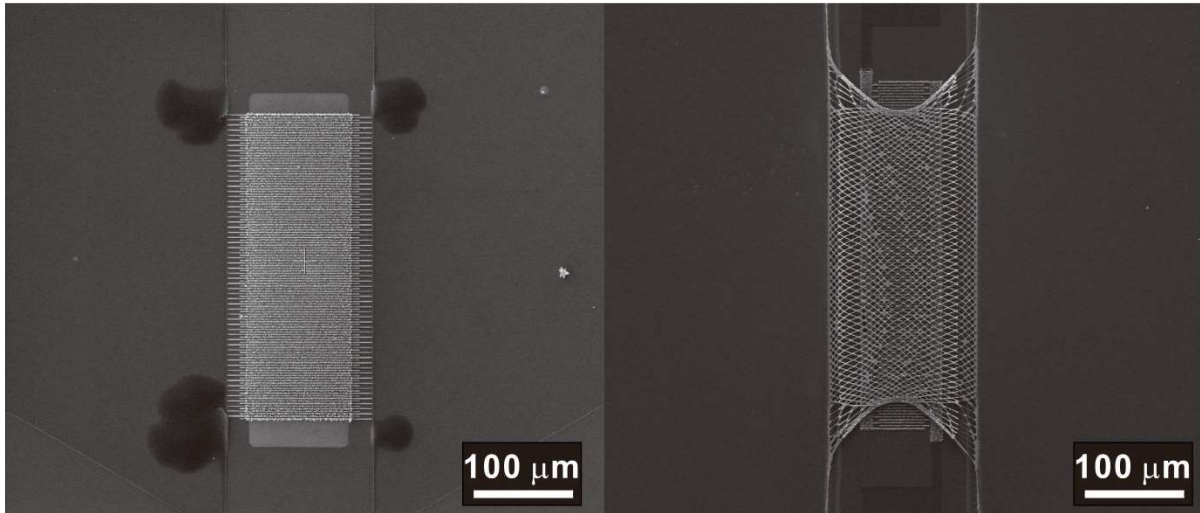


Figure 24. Scanning electron microscopy (SEM) image of interdigitated array electrode and sandwich electrodes which show the geometry of electrode structures used in the experiments.

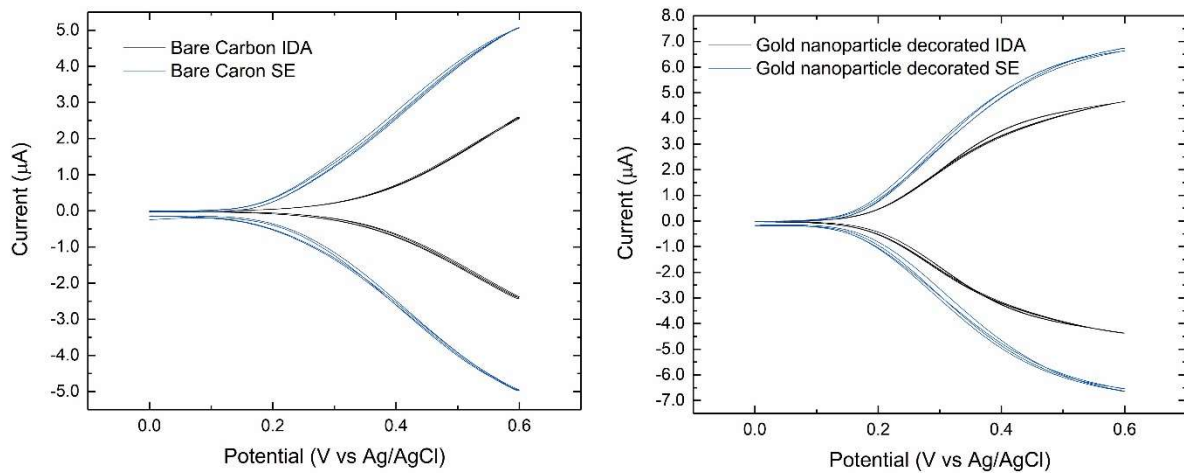


Figure 25. Dual mode cyclic voltammetry (CV) graph of interdigitated array (IDA) electrode and sandwich electrode (SE) for both carbon and gold electrodeposited electrodes. SE showed superior current level in CV despite the fact that IDA have larger sensor operation area.

	Sensor operation area	Electrode gap	Redox cycling current		Redox cycling efficiency	
			Carbon	Gold nanoparticle decorated	Carbon	Gold nanoparticle decorated
IDA	27000 μm^2	2 μm	2.591 μA	4.653 μA	95.963 A/m^2	172.333 A/m^2
SE	21000 μm^2	1.8 μm	5.065 μA	6.635 μA	241.190 A/m^2	315.952 A/m^2

Table 1. Comparison in IDA and SE structure in terms of geometry and CV properties.

3.3 Gold nanoparticle electrodeposition optimization

3.3.1 Electrodeposition condition

From numerous trials of gold electrodeposition, gold nanoparticles tended to grow better on edge of the carbon electrode. This empirical observation is explained by concentrated electric field at sharp edged. [43] As the pyrolyzed carbon structure is formed by volume shrinkage, carbon electrode edge shows very sharp angle along the edge. This may have intensified the electric field concentration effect for electrodeposition of gold particle.

Under same electrodeposition condition, the gold nanoparticles were more conformally deposited to electrode structure that have many edges such as IDA or suspended mesh electrode compared to planar electrode. The gold nanoelectrodes are primarily deposited to the edge of carbon electrodes and the edges functioned as the guide of particle deposition. For conformal deposition of gold nanoparticles, IDA was used as bottom electrode instead of planar electrode. Figure 26 shows the SEM image of gold nanoparticle deposition of IDE and planar electrode. As can be observed in the image, the gold particles are more conformally deposited along IDE structure compared to planar electrode

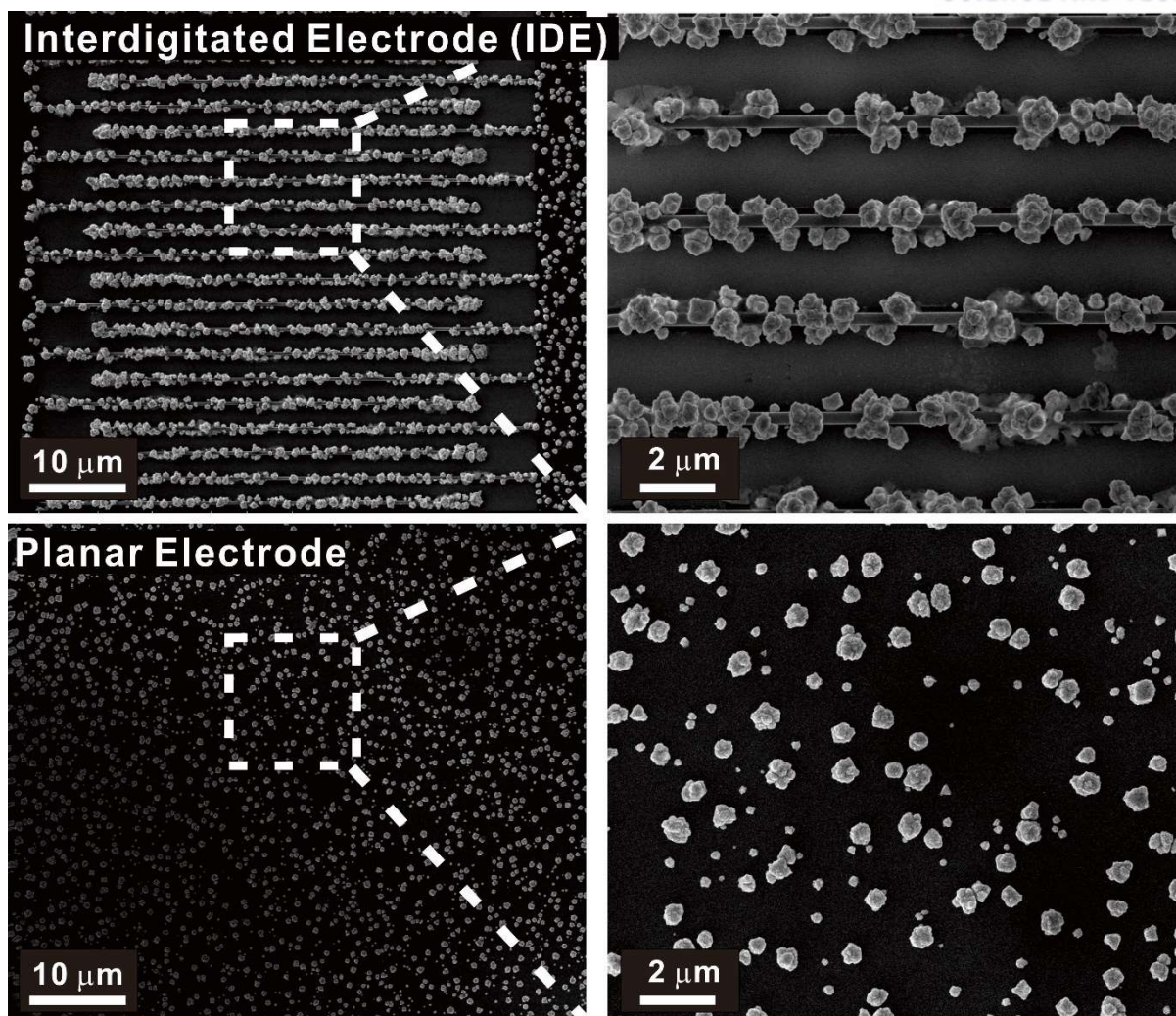


Figure 26. Scanning electron microscopy (SEM) image of gold nanoparticle deposition result on IDE and planar electrode. Both electrodes experienced 20 seconds of $-1.3V$ vs $Ag/AgCl$ as nucleation step and 40 seconds of $-0.9V$ vs $Ag/AgCl$ as particles growth step. Gold particles were more reliably deposited on IDE.

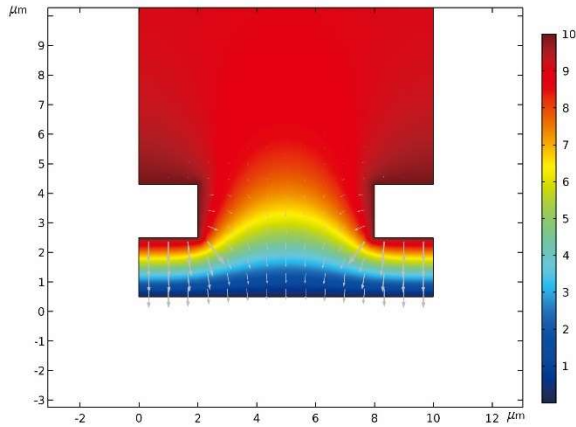
3.3.2 IDE as bottom electrode compared to planar electrode

Comparing planar electrode and IDE as the bottom electrode of sandwich structure, although gold particles are more conformally deposited in IDE, the planar electrode have larger surface area compared to IDE. Simulation using COMSOL program was conducted to check whether choosing IDE as bottom electrode is more effective for the sandwich electrode structure.

As the efficiency of electrode structures was meant to be compared in bulk solution, the simulation stage was set as large rectangle of width $10\mu\text{m}$ and height of $800\mu\text{m}$. At time $t = 0$, the bulk solution was filled with 10mM Ferrocyanide solution. The boundary condition of background top corner was set to show constant ferrocyanide concentration of 10mM . The surface of generator electrode, the bottom electrode, was calculated to remove ferrocyanide and replace it to ferricyanide according to ferrocyanide reaction speed, voltage applied to generator electrode and the adjacent ferrocyanide concentration to electrode surface. The surface of collector electrode, the suspended mesh electrode, was calculated to remove ferricyanide and replace it to ferrocyanide according to ferricyanide reaction speed and the adjacent ferricyanide concentration to electrode surface. The mesh for simulation computation was formed in triangular shape (Element size = $0.001 - 3\mu\text{m}$, maximum element growth rate = 1.1, curvature factor = 0.2, resolution of narrow regions = 5). The simulation was conducted in time dependent computation in the range of 0 to 32 seconds which the time step of 0.1 seconds. The voltage scan was given to generator electrode from 0 to 0.8V with scan rate 0.05 V/s .

How the redox cycling between two electrodes are performed can be examined from ferrocyanide concentration distribution graph. As shown in Figure 27, the ferrocyanide concentration and flow graph is similar for both sandwich electrodes. Although the distance between bottom electrode and suspended mesh are set to be same for both structures, the actual electrode gap which governs the area of redox cycling between planar bottom electrode and mesh seems to be smaller than IDE bottom electrode. The redox cycling efficiency was numerically measured by calculating total flux magnitude of collector electrode, which can be only resulted from redox cycling. As shown in Figure 28, the total flux magnitude of collector electrode is $19\text{ nmol}/(\text{m}\cdot\text{sec})$ for IDE bottom electrode and $22\text{ nmol}/(\text{m}\cdot\text{sec})$ for planar bottom electrode. Although the electrode structure with planar bottom electrode showed higher flux magnitude, the difference between two structures may not be significant.

Planar electrode



Interdigitated electrode (IDE)

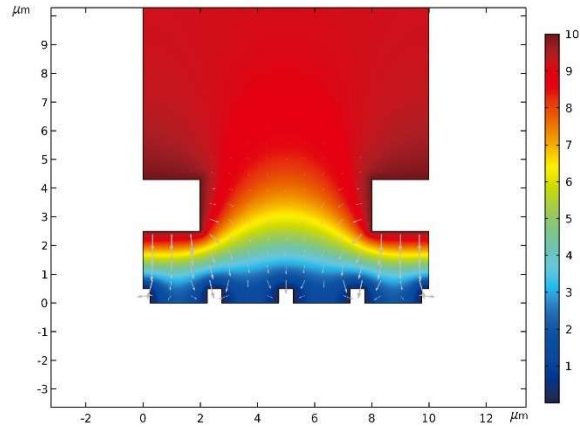
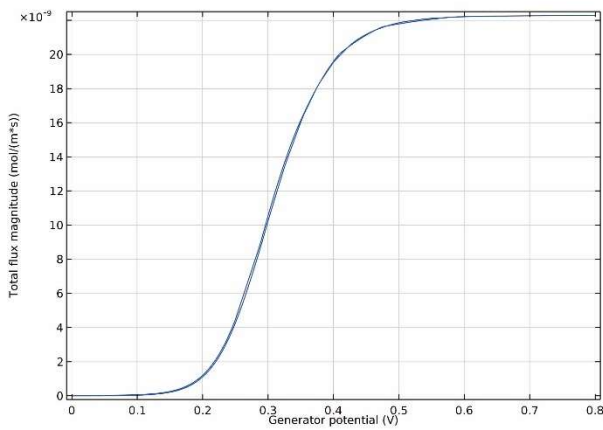


Figure 27. Plot of ferrocyanide concentration distribution (color distribution) and relative flux velocity (gray arrows) around the electrode surface. The different color can be interpreted in to ferrocyanide concentration in mM through color legend. The ferrocyanide transportation is mainly occurred between the generator and collector electrodes.

Planar electrode



Interdigitated electrode (IDE)

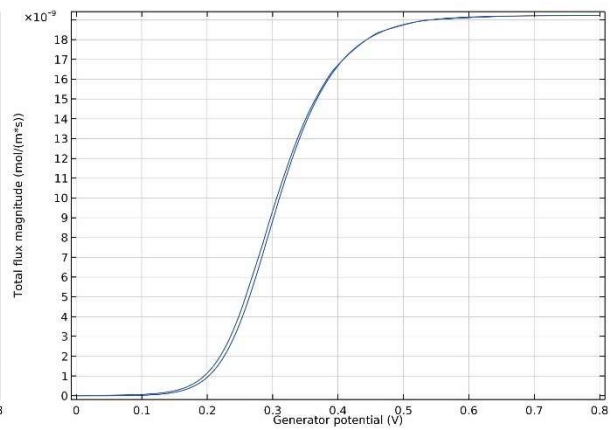


Figure 28. The total flux magnitude collected in collector electrode is plotted in terms of generator potential to compare the redox cycling efficiency of two electrode structures.

3.4 Uric acid sensing performance of this work

The uric acid sensing performance was evaluated for three types of sensor structures. (Figure 29) Type A is interdigitated array (IDA) structure with one comb selectively immobilized with uricase enzyme. Type B is sandwich electrode (SE) with uricase enzyme selectively immobilized to suspended mesh electrode (SME). Type C is SE with uricase enzyme selectively immobilized to interdigitated bottom electrode (IDE). The sensing result of type A was evaluated to compare sensing performance of IDA structure and SE structure. The sensing result of type B and C was compared to see among SME and IDE, which electrode is more appropriate to be used as uric acid sensing. As surface reactivity severely deteriorated after selective immobilization of uricase enzyme, the sensing was performed only with un-modifying electrodes.

The sensing was conducted by chronoamperometric test of 0.6V vs Ag/AgCl according to each uric acid concentration. The representative value was organized in uric acid concentration – current signal graph as shown in Figure 30. The uric acid concentration was measured from 0 μM to 1000 μM and to improve visibility of the graph, the concentration-signal graph was divided according to uric acid concentration; low concentration graph of 0 to 100 μM and high concentration graph of 100 to 1000 μM . The overall amplitude of current signal was highest with type C and lowest with Type A. The graphs of three types of sensor did not cross each other for high concentration but for low concentration, the graph of type A crossed the graph of type B around uric acid concentration of 30 μM .

The sensing performance was compared in two factors, lower limit of detection, shorten as LOD (μM) and sensitivity ($\mu\text{A}/(\text{mM}\cdot\text{cm}^2)$) (Table 2). LOD and sensitivity of sensors were calculated individually for low concentration and high concentration. The LOD was highest with IDA structure (type A) for both low concentration range and high concentration range. The lowest LOD was shown with type B for low concentration range but type C showed lowest LOD for high concentration range. The sensitivity was calculated as current difference per uric acid concentration difference divided by sensor operation area. Since the IDA and SE have different sensor operation area and operation area is proportional to current amplification, the sensitivity value was divided with sensor operation area for better evaluation. SE structure showed better sensitivity compared to IDA structure. The sensitivity was improved when SME was used for sensing (type C) than IDE (type B).

By summarizing the result, the SE structure showed better sensing performance than IDA for both LOD and sensitivity. The result can be explained from the facing area of enzyme

immobilized electrode and sensing electrode as it governs the hydrogen peroxide material transportation from enzyme to sensing electrode. For sandwich electrode, the enzyme immobilized electrode and sensing electrode face each other all across the sensor operation area while it is limited in IDA.

Among SE structures, enzyme immobilized on IDE and current sensed with SME (type C) showed better result compared to enzyme immobilized on SME and current sensed with IDE (type B). This can be explained with mass transportation of hydrogen peroxide. When enzyme is immobilized on SME, the enzyme is not only deposited on the bottom surface of SME, where SME and IDE are facing, but also on the top surface of SME. The hydrogen peroxide which occurs from bottom surface enzyme is likely to reach IDE but that from top surface enzyme have high chance to be diffused to bulk solution. When enzyme is immobilized to IDE, since SME is covering over IDE, there is low chance for hydrogen peroxide to be diffused out to bulk without passing SME. Therefore, sensing the current signal with SME showed better sensor performance.

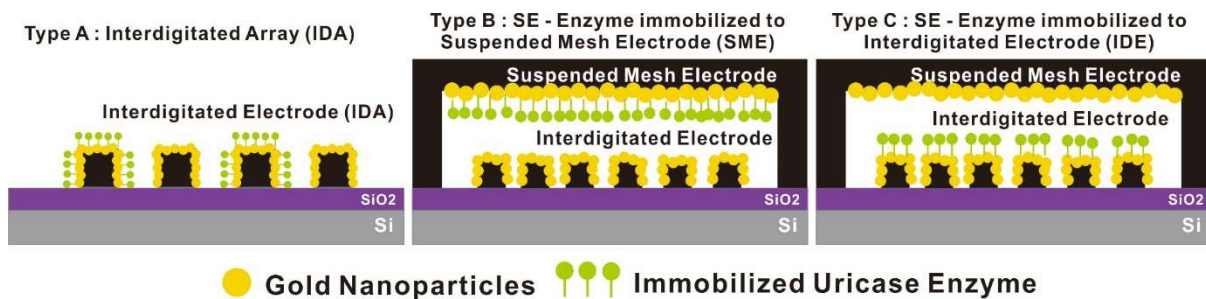


Figure 29. Schematic of three different types of uric acid sensor structures. Type A is interdigitated array (IDA) structure with one comb selectively immobilized with uricase enzyme. Type B is sandwich electrode (SE) with uricase enzyme selectively immobilized to suspended mesh electrode (SME). Type C is SE with uricase enzyme selectively immobilized to interdigitated bottom electrode (IDE).

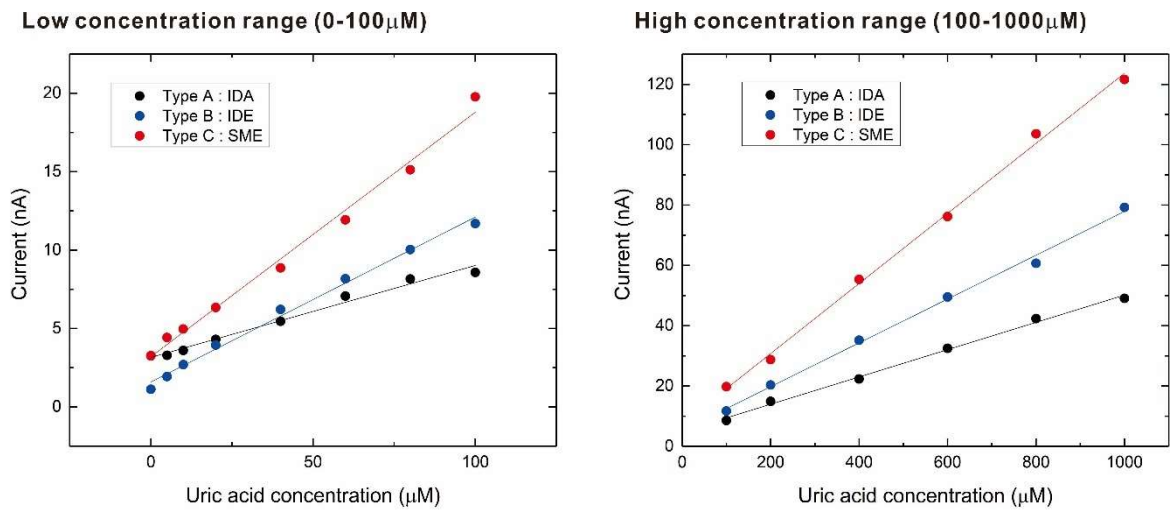


Figure 30. Amperometric current responses from three independent uric acid sensor structures are plotted in terms of uric acid concentration. (Black circles: IDA structure, type A; blue circles: SE structure with current signal sensed with IDE, type B; red circles: SE structure with current signal sensed with SME, type C)

	0 - 100 μM			100 - 1000 μM		
	LOD (μM)	Sensitivity ($\text{A}/\mu\text{M}$)	Sensitivity ($\mu\text{A}/(\text{mM}\cdot\text{cm}^2)$)	LOD (μM)	Sensitivity ($\text{A}/\mu\text{M}$)	Sensitivity ($\mu\text{A}/(\text{mM}\cdot\text{cm}^2)$)
Type A	7.91	$5.86\text{E}-11$	217.14	58.23	$4.52\text{E}-11$	167.41
Type B	5.33	$1.05\text{E}-10$	500.74	53.76	$7.26\text{E}-11$	345.91
Type C	6.25	$1.56\text{E}-10$	742.11	46.74	$1.16\text{E}-10$	553.26

Table 2. Comparison in sensing performance between three types of uric acid sensing structures. The sensing performance was evaluated with low limit of detection and sensitivity in uric acid detection.

IV Conclusion and future works

Through this work, uric acid sensor with high performance was developed based on carbon sandwich electrode decorated with gold nanoparticles. The sensor was evaluated with wide uric acid concentration of 5 to 1000 μM and showed high sensitivity of $742.11 \mu\text{A}/(\text{mM}\cdot\text{cm}^2)$ for low concentration range and $553.26 \mu\text{A}/(\text{mM}\cdot\text{cm}^2)$ for high concentration range. Lower limit of detection was measured to be $6.25 \mu\text{M}$. The carbon sandwich electrode is constitute of bottom interdigitated electrode (IDE) and suspended mesh electrode (SME). The carbon electrodes are fabricated with batch process using carbon-MEMS technique, PECVD, and BOE wet etching. The sandwich carbon electrode was decorated with gold nanoparticles by two steps electrodeposition. Uric acid sensing was conducted using catalytic reaction including uricase enzyme. As uric acid is converted in to allantoin by uricase enzyme, water molecule is oxidized to hydrogen peroxide which is detected to show uric acid concentration. The uricase enzyme was selectively immobilized to IDE to maintain the surface reactivity of SME, which was used for hydrogen peroxide sensing. The high sensitivity of sandwich electrode was possible due to wide IDE and SME facing area and small gap between two electrodes which helps mass transportation of hydrogen peroxide from enzyme to sensing electrode. Although the interference test and serum test is left to be conducted, as the sensing method include enzymatic sensing without mediator, the sensor is believed to selectively detect uric acid concentration in presence of other biomaterials.

The sandwich electrode structure shows better redox cycling efficiency compared to interdigitated array electrode structure which was previously used in selective immobilized enzymatic biosensor. The sandwich electrode structure can be utilized as other type of biosensors as enzyme selective immobilization method used in this work can be applied with the other enzyme immobilization beside the uricase enzyme. Various methods were implemented to improve the sensor structure properties such as carbon-MEMS technique and gold nanoparticle deposition. Through carbon-MEMS technique, sandwich structure with small gap between two electrode set was successfully reproducible. Through gold nanoparticle deposition, the electrode surface reactivity was improved as surface area and electrode conductivity increase.

Future work with the gold nanoparticle decorated sandwich electrode uric acid sensor is to design superior sensing mechanism of utilizing redox cycling and to construct multiple sensor. The uric acid sensor in this work collect the current signal from the byproduct of enzymatic reaction, hydrogen peroxide by decomposing it. The current signal can be extremely multiplied when the byproduct can work as redox cycling mediator, which repeats oxidation and reduction. As three sets of individual electrodes are closely located in the sandwich electrode, it is possible to

selectively immobilize the enzyme on one electrode and collect current signal by redox cycling with remaining two electrodes.

References

1. Sautin, Y. Y., and Johnson, R. J. (2008). Uric acid: the oxidant-antioxidant paradox. *Nucleosides, Nucleotides, and Nucleic Acids*, 27(6-7), 608-619.
2. Liu, D., Yun, Y., Yang, D., Hu, X., Dong, X., Zhang, N., ... and Duan, W. (2019). What Is the Biological Function of Uric Acid? An Antioxidant for Neural Protection or a Biomarker for Cell Death. *Disease markers*, 2019.
3. Cammalleri, L., and Malaguarnera, M. (2007). Rasburicase represents a new tool for hyperuricemia in tumor lysis syndrome and in gout. *International journal of medical sciences*, 4(2), 83.
4. Pellecchia, M. T., Savastano, R., Moccia, M., Picillo, M., Siano, P., Erro, R., ... and Barone, P. (2016). Lower serum uric acid is associated with mild cognitive impairment in early Parkinson's disease: a 4-year follow-up study. *Journal of Neural Transmission*, 123(12), 1399-1402.
5. Vargas-Bernal, R., Rodríguez-Miranda, E., and Herrera-Pérez, G. (2012). Evolution and expectations of enzymatic biosensors for pesticides. *Pesticides-Advances in Chemical and Botanical Pesticides*.
6. Pileggi, V. J., Di Giorgio, J., and Wybenga, D. K. (1972). A one-tube serum uric acid method using phosphotungstic acid as protein precipitant and color reagent. *Clinica Chimica Acta*, 37, 141-149.
7. Folin, O., and Denis, W. (1912). A new (colorimetric) method for the determination of uric acid in blood. *J. biol. Chem*, 13(469), 1912-13.
8. Henry, R. J. (1957). Sobel C, Kim J. A modified carbonate phosphotungstate method for the determination of uric acid, and comparison with the spectrophotometric uricase method. *Am J Clin Pathol*, 28, 152-160.
9. Wheat, J. L. (1968). Determination of Uric Acid An Automated Phosphotungstate Method Using NaOH as the Alkali. *Clinical chemistry*, 14(7), 630-636.
10. Caraway, W. T. (1955). Determination of uric acid in serum by a carbonate method. *American Journal of Clinical Pathology*, 25(7_ts), 840-845.

11. Sanghavi, B. J., Mobin, S. M., Mathur, P., Lahiri, G. K., and Srivastava, A. K. (2013). Biomimetic sensor for certain catecholamines employing copper (II) complex and silver nanoparticle modified glassy carbon paste electrode. *Biosensors and Bioelectronics*, 39(1), 124-132.
12. Azmi, N. E., Ramli, N. I., Abdullah, J., Hamid, M. A. A., Sidek, H., Rahman, S. A., ... and Yusof, N. A. (2015). A simple and sensitive fluorescence based biosensor for the determination of uric acid using H₂O₂-sensitive quantum dots/dual enzymes. *Biosensors and Bioelectronics*, 67, 129-133.
13. Zhang, T., Sun, X., and Liu, B. (2011). Synthesis of positively charged CdTe quantum dots and detection for uric acid. *Spectrochimica Acta Part A: Molecular and Biomolecular Spectroscopy*, 79(5), 1566-1572.
14. Xu, M., Gao, Z., Zhou, Q., Lin, Y., Lu, M., and Tang, D. (2016). Terbium ion-coordinated carbon dots for fluorescent aptasensing of adenosine 5'-triphosphate with unmodified gold nanoparticles. *Biosensors and Bioelectronics*, 86, 978-984.
15. Pradhan, T., Maiti, S., Kumar, R., Lee, Y. H., Kim, J. W., Lee, J. H., and Kim, J. S. (2015). Rationally designed non-enzymatic fluorogenic 'turn-on' probe for uric acid. *Dyes and Pigments*, 121, 1-6.
16. Türkeş, C., Arslan, M., Demir, Y., Çoçaj, L., Nixha, A. R., and Beydemir, Ş. (2019). Synthesis, biological evaluation and in silico studies of novel N-substituted phthalazine sulfonamide compounds as potent carbonic anhydrase and acetylcholinesterase inhibitors. *Bioorganic chemistry*, 89, 103004.
17. Hou, P., Wang, J., Fu, S., Liu, L., and Chen, S. (2019). Highly sensitive fluorescent probe based on a novel phenothiazine dye for detection of thiophenols in real water samples and living cells. *Analytical and bioanalytical chemistry*, 411(4), 935-942.
18. Dias, A. N., da Silva, A. C., Simão, V., Merib, J., and Carasek, E. (2015). A novel approach to bar adsorptive microextraction: Cork as extractor phase for determination of benzophenone, triclocarban and parabens in aqueous samples. *Analytica chimica acta*, 888, 59-66.
19. Jiang, J., and Du, X. (2014). Sensitive electrochemical sensors for simultaneous determination of ascorbic acid, dopamine, and uric acid based on Au@ Pd-reduced graphene oxide nanocomposites. *Nanoscale*, 6(19), 11303-11309.

20. Ahuja, T., Mir, I. A., and Kumar, D. (2007). Biomolecular immobilization on conducting polymers for biosensing applications. *Biomaterials*, 28(5), 791-805.
21. Peng, B., Cui, J., Wang, Y., Liu, J., Zheng, H., Jin, L., ... and Wu, Y. (2018). CeO_{2-x}/C/rGO nanocomposites derived from Ce-MOF and graphene oxide as a robust platform for highly sensitive uric acid detection. *Nanoscale*, 10(4), 1939-1945.
22. Devi, R., and Pundir, C. S. (2014). Construction and application of an amperometric uric acid biosensor based on covalent immobilization of uricase on iron oxide nanoparticles/chitosan-g-polyaniline composite film electrodeposited on Pt electrode. *Sensors and Actuators B: Chemical*, 193, 608-615.
23. Ali, S. M. U., Ibupoto, Z. H., Kashif, M., Hashim, U., and Willander, M. (2012). A potentiometric indirect uric acid sensor based on ZnO nanoflakes and immobilized uricase. *Sensors*, 12(3), 2787-2797.
24. Umasankar, Y., Periasamy, A. P., and Chen, S. M. (2010). Poly (malachite green) at nafion doped multi-walled carbon nanotube composite film for simple aliphatic alcohols sensor. *Talanta*, 80(3), 1094-1101.
25. Lin, K. C., Huang, J. Y., and Chen, S. M. (2013). Enhancing electro-codeposition and electrocatalytic properties of poly (neutral red) and FAD to determine NADH and H₂O₂ using amino-functionalized multi-walled carbon nanotubes. *RSC Advances*, 3(48), 25727-25734.
26. Yogeswaran, U., and Chen, S. M. (2007). Separation and concentration effect of f-MWCNTs on electrocatalytic responses of ascorbic acid, dopamine and uric acid at f-MWCNTs incorporated with poly (neutral red) composite films. *Electrochimica Acta*, 52(19), 5985-5996.
27. Joshi, P. P., Merchant, S. A., Wang, Y., and Schmidtke, D. W. (2005). Amperometric biosensors based on redox polymer- carbon nanotube- enzyme composites. *Analytical Chemistry*, 77(10), 3183-3188.
28. Wang, J. (2005). Carbon-nanotube based electrochemical biosensors: A review. *Electroanalysis: An International Journal Devoted to Fundamental and Practical Aspects of Electroanalysis*, 17(1), 7-14.
29. Shao, Y., Wang, J., Wu, H., Liu, J., Aksay, I. A., and Lin, Y. (2010). Graphene based electrochemical sensors and biosensors: a review. *Electroanalysis: An International Journal Devoted to Fundamental and Practical Aspects of Electroanalysis*, 22(10), 1027-1036.

30. Liu, G., and Lin, Y. (2006). Amperometric glucose biosensor based on self-assembling glucose oxidase on carbon nanotubes. *Electrochemistry Communications*, 8(2), 251-256.
31. Gooding, J. J., Wibowo, R., Liu, J., Yang, W., Losic, D., Orbons, S., ... and Hibbert, D. B. (2003). Protein electrochemistry using aligned carbon nanotube arrays. *Journal of the American Chemical Society*, 125(30), 9006-9007.
32. Sharma, D., Lim, Y., Lee, Y., and Shin, H. (2015). Glucose sensor based on redox-cycling between selectively modified and unmodified combs of carbon interdigitated array nanoelectrodes. *Analytica chimica acta*, 889, 194-202.
33. Sharma, D., Lee, J., Seo, J., and Shin, H. (2017). Development of a sensitive electrochemical enzymatic reaction-based cholesterol biosensor using nano-sized carbon interdigitated electrodes decorated with gold nanoparticles. *Sensors*, 17(9), 2128.
34. Sharma, D., Lee, J., and Shin, H. (2018). An electrochemical immunosensor based on a 3D carbon system consisting of a suspended mesh and substrate-bound interdigitated array nanoelectrodes for sensitive cardiac biomarker detection. *Biosensors and Bioelectronics*, 107, 10-16.
35. Singh, B., Lohan, S., Sandhu, P. S., Jain, A., and Mehta, S. K. (2016). Functionalized carbon nanotubes and their promising applications in therapeutics and diagnostics. In *Nanobiomaterials in Medical Imaging* (pp. 455-478). William Andrew Publishing.
36. Gooding, J. J., Wibowo, R., Liu, J., Yang, W., Losic, D., Orbons, S., ... and Hibbert, D. B. (2003). Protein electrochemistry using aligned carbon nanotube arrays. *Journal of the American Chemical Society*, 125(30), 9006-9007.
37. Lin, Y., Lu, F., Tu, Y., and Ren, Z. (2004). Glucose biosensors based on carbon nanotube nanoelectrode ensembles. *Nano letters*, 4(2), 191-195.
38. Kassegne, S., Vomero, M., Gavuglio, R., Hirabayashi, M., Özyilmaz, E., Nguyen, S., ... and Khosla, A. (2015). Electrical impedance, electrochemistry, mechanical stiffness, and hardness tunability in glassy carbon MEMS μ ECOG electrodes. *Microelectronic Engineering*, 133, 36-44.
39. Heo, J. I., Shim, D. S., Teixidor, G. T., Oh, S., Madou, M. J., and Shin, H. (2011). Carbon interdigitated array nanoelectrodes for electrochemical applications. *Journal of the Electrochemical Society*, 158(3), J76-J80.

40. Mandon, C. A., Blum, L. J., and Marquette, C. A. (2009). Aryl diazonium for biomolecules immobilization onto SPRi chips. *ChemPhysChem*, 10(18), 3273-3277.
41. Belanger, D., and Pinson, J. (2011). Electrografting: a powerful method for surface modification. *Chemical Society Reviews*, 40(7), 3995-4048.
42. Jin, D., Seo, M. H., Huy, B. T., Pham, Q. T., Conte, M. L., Thangadurai, D., and Lee, Y. I. (2016). Quantitative determination of uric acid using CdTe nanoparticles as fluorescence probes. *Biosensors and Bioelectronics*, 77, 359-365.
43. Kim, S., Dong, W. J., Gim, S., Sohn, W., Park, J. Y., Yoo, C. J., ... and Lee, J. L. (2017). Shape-controlled bismuth nanoflakes as highly selective catalysts for electrochemical carbon dioxide reduction to formate. *Nano Energy*, 39, 44-52.

Acknowledgement

I express sincere and deep gratitude to my advisor, Professor Heungjoo Shin. He provided the opportunity and guidance to start and improve my research throughout the master's course. He has taught me the methodology to be carried out in the research with great endurance. I believe I would not have finished this thesis without his support. I would also like to appreciate great thanks to the committee members, Professor Jaesung Jang and Professor Hoon Eui Jeong for the suggestions and assistances given during the thesis presentation. Thanks to their assistance, I could successfully complete this thesis.

I am extremely grateful to all the members of MNIS Lab members including the graduated seniors, Dr. Deepti Sharma, Dr. Yeongjin Lim, Dr. Police Anil Kuma Reddy, Dr. Pijus Kundu, Jongmin Lee, Beomsang Kim, Seungwook Lee, Taejung Kim, and Wootaek Cho for their warm help during my master's course in UNIST. Special appreciation is given to Jongmin Lee who had deeply assisted me throughout the research. Owing to the assistance of all the lab members, I was able to have great time during the master's course.

I am very thankful for my friends, Seungho Baek, Songhyun Kim, Dawn Jeong, Seunghwan Lee, Hyukjun Joo, Daewook Kim, who have made my days in UNIST. The sincere love is given to my family, Ogyoung Jung, Bokyung Oh, Sangho Jung, who have given endless support and been my home when I needed the rest.